



1
2 DOCTORAL THESIS

3
4 Optimisation studies and background
5 estimation in searches for the supersymmetric
6 partner of the top quark in all-hadronic final
7 states with the ATLAS Detector at the LHC

8
9 A thesis submitted in fulfillment of the requirements
10 for the degree of Doctor of Philosophy

11 in the

12 Experimental Particle Physics Research Group
13 School of Mathematical and Physical Sciences

14 Author:
15 Fabrizio MIANO

Supervisor:
Dr. Fabrizio SALVATORE

15th November 2017

Dedicated to my family.

*Have no fear for atomic energy
'cause none of them can stop the
time*

17

Robert Nesta Marley

18

Acknowledgments

- 19 Thanks to every single thing that went wrong. It made me stronger.

Declaration

21 I, Fabrizio MIANO, hereby declare that this thesis, titled, "Optimisation studies and back-
22 ground estimation in searches for the supersymmetric partner of the top quark in all-
23 hadronic final states with the ATLAS Detector at the LHC" has not been and will not be,
24 submitted in whole or in part to another University for the award of any other degree.

25 *Brighton, 15th November 2017*

27 University of Sussex
28 School of Mathematical and Physical Sciences
29 Experimental Particle Physics Research Group

30 Doctoral Thesis

31

32 Optimisation studies and background estimation in searches for
33 the supersymmetric partner of the top quark in all-hadronic final
34 states with the ATLAS Detector at the LHC
35

36 by Fabrizio MIANO

37 *Abstract*

38 This thesis presents searches for supersymmetry in $\sqrt{s} = 13$ TeV proton-proton collisions
39 at the LHC using data collected by the ATLAS detector in 2015, 2016 and 2017. Events
40 with 4 or more jets and missing transverse energy were selected. Kinematic variables were
41 investigated and optimisations were performed to increase the sensitivity to supersym-
42 metric signals. Standard Model backgrounds were estimated by means of Monte Carlo
43 simulations and data-driven techniques. Before analysing the data in the blinded signal
44 regions the agreement between data and background predictions and the extrapolations
45 from control and validation regions to signal regions were validated. The analysis yiel-
46 ded no significant excess in any of the analyses performed. Therefore limits were set and
47 the results were interpreted as lower bounds on the masses of supersymmetric particles
48 in various scenarios and models.

⁴⁹ Contents

⁵⁰	Introduction	1
⁵¹	1 Theoretical Framework of Supersymmetry searches	2
⁵²	1.1 The Standard Model	2
⁵³	1.1.1 Electroweak Symmetry Breaking and the Higgs mechanism	6
⁵⁴	1.1.2 Flaws of the Standard Model	8
⁵⁵	1.2 Supersymmetry	10
⁵⁶	1.2.1 Why SUSY?	11
⁵⁷	1.2.2 Minimal Supersymmetric Standard Model	12
⁵⁸	1.2.3 Supersymmetry Phenomenology	14
⁵⁹	2 The ATLAS Experiment at the LHC	20
⁶⁰	2.1 The LHC	20
⁶¹	2.2 The ATLAS Detector	23
⁶²	2.2.1 The Magnet System	24
⁶³	2.2.2 The Inner Detector	25
⁶⁴	2.2.3 The Calorimeters	28
⁶⁵	2.2.4 The Muon Spectrometer	29
⁶⁶	2.3 The ATLAS Trigger System	31
⁶⁷	2.3.1 Level 1 Trigger	32
⁶⁸	2.3.2 High-Level Trigger	32
⁶⁹	3 The <i>b</i>-jet Trigger Signature in ATLAS	34
⁷⁰	3.1 Trigger Efficiency	34
⁷¹	4 Event Simulation and Reconstruction	35
⁷²	4.1 Event Generation	35
⁷³	4.1.1 Parton Distribution Functions (PDFs)	35

74	4.1.2 Matrix Element Calculation	35
75	4.1.3 Parton Showers	35
76	4.1.4 Hadronisation	35
77	4.2 Detector Simulation	35
78	5 Stop searches in final states with jets and missing transverse energy	36
79	6 Results and Statistical Intepretations	37
80	Trigger	38
81	Bibliography	39

⁸² List of Tables

⁸³	1.1 Forces and mediators described by the SM	5
⁸⁴	1.2 SUSY particles in the MSSM	15
⁸⁵	1.3 Parameters in the pMSSM.	16

⁸⁶ List of Figures

⁸⁷ 1.1	The Higgs potential in the complex plane.	8
⁸⁸ 1.2	Summary of several Standard Model total production cross-section measurements, corrected for leptonic branching fractions, compared to the corresponding theoretical expectations. All theoretical expectations were calculated at NLO or higher. The luminosity used for each measurement is indicated close to the data point. Uncertainties for the theoretical predictions are quoted from the original ATLAS papers. They were not always evaluated using the same prescriptions for PDFs and scales. Not all measurements are statistically significant yet [1].	9
⁹⁵ 1.3	The inverse couplings of electromagnetic (dashed blue), weak (dashed red) and strong (solid green) interactions with the SM (left) and a supersymmetric model (right). In the SM the three lines do not meet at one point, but with the introduction of supersymmetry, and assuming that the supersymmetric particles are not heavier than about 1 TeV, they do meet. This is an indication that supersymmetry could be discovered at the LHC.	12
⁹⁶ 1.4	NLO+NLL production cross-sections as a function of mass at $\sqrt{s} = 13\text{TeV}$ [2]	17
¹⁰³ 1.5	Illustration of stop decay modes in the $(m_{\tilde{t}_1}, m_{\tilde{\chi}_1^0})$ mass place where the $\tilde{\chi}_1^0$ is assumed to be the lightest supersymmetric particle. The dashed blue lines indicate thresholds separating regions where different processes dominate.	18
¹⁰⁶ 1.6	Diagrams of the decay topologies of the signal models considered in this work. The term "soft" refers to decay products that have transverse momenta below the detector thresholds.	19
¹⁰⁹ 2.1	CERN Accelerator complex. The LHC is the last ring (dark grey line). Smaller machines are used for early-stage acceleration and also to provide beams for other experiments [3].	22

112	2.2 Cut-away view of the ATLAS detector. The dimensions of the detector are	
113	25 m in height and 44 m in length. The overall weight of the detector is	
114	approximately 7000 tonnes [3].	23
115	2.3 The ATLAS magnet system.	25
116	2.4 The ATLAS Inner Detector	26
117	2.5 A computer generated image of the full calorimeter.	28
118	2.6 Cut-away view of the ATLAS muon system [4].	30
119	2.7 The ATLAS TDAQ system. L1Topo and FTK were being commissioned	
120	during 2015 and not used for the results shown in this thesis [5].	31

¹²¹ Introduction

¹²² Last thing to write

¹²³ **1** | ¹²⁴ **Theoretical Framework of Super-**
¹²⁵ **symmetry searches**

A theory is something nobody believes, except the person who made it. An experiment is something everybody believes, except the person who made it.

Albert Einstein

¹²⁶ The Standard Model (SM) of particle physics is an effective theory that aims to provide
¹²⁷ a general description of fundamental particles and the phenomena we see in nature, i. e.
¹²⁸ the way they interact. Unfortunately, our understanding of nature is still limited due to
¹²⁹ some opened question to which the SM is not able to answer to, yet.

¹³⁰ In this chapter, an overview of the SM will be presented in Section 1.1 together with
¹³¹ the limitations of such theory and some of the reasons behind the need of an extension.
¹³² For the last decades theoretical physicsts have been trying to provide extensions to the
¹³³ SM, the so-called beyond-the-SM theories. Among these, one of the most popular, Super-
¹³⁴ symmetry which will be discussed in Section 1.2.

¹³⁵ 1.1 The Standard Model

¹³⁶ The 20th century can be considered a quantum revolution. Several experiments led to
¹³⁷ discoveries which were found to be, together with the formalised theory, a solid base of
¹³⁸ the Standard Model of particle physics and our description of nature. Several particles
¹³⁹ were predicted first by the SM and then experimentally observed e. g. the W and the Z
¹⁴⁰ bosons, the τ lepton, [6], and more recently the Higgs boson at the LHC discovered by
¹⁴¹ ATLAS [7] and CMS [8].

¹⁴² The SM lays on a Quantum Field Theory (QFT) where particles are treated like fields.
¹⁴³ It can describe three of the four fundamental forces; weak, electromagnetic, and strong.
¹⁴⁴ As of today, gravity is not considered in the SM. Sections 1.1 and 1.1.2 will be focused
¹⁴⁵ on the description of the fields together with the carriers of the information, and on the
¹⁴⁶ limitations that such theory implies, respectively.

¹⁴⁷ The most general classification of the particles within the SM can be made by means of
¹⁴⁸ spin. Fermions have half-integer spin values - and are usually referred to as matter -, and
¹⁴⁹ bosons have integer-spin values. A noteworthy subset of bosons is formed by the Spin-1
¹⁵⁰ bosons (also known as gauge bosons). These can be considered the information carriers
¹⁵¹ or, in fact, the mediators of the forces.

¹⁵² Fermions

¹⁵³ Six quarks and six leptons belong to the fermions family. In particular, fermions can be
¹⁵⁴ grouped into three generations. Each generation contains four particles; one up- and one
¹⁵⁵ down-type quark, one charged lepton and one neutral lepton. The masses of the charged
¹⁵⁶ leptons and quarks increase with the generation. The six quarks of the SM can be grouped
¹⁵⁷ into three doublets:

$$\begin{pmatrix} u \\ d \end{pmatrix}, \quad \begin{pmatrix} c \\ s \end{pmatrix}, \quad \begin{pmatrix} t \\ b \end{pmatrix}$$

¹⁵⁸ The up-type quarks (up, charm, top) have charge $+\frac{2}{3}e$ and the down-type quarks (down,
¹⁵⁹ strange, beauty/bottom) have charge $-\frac{1}{3}e$, where e is the electron charge. Quarks also
¹⁶⁰ have another quantum number that can be seen as the analogue of the electric charge,
¹⁶¹ which is the colour charge. This can exist in three different states; "red", "green" and
¹⁶² "blue". Moreover, as a consequence of *confinement*, which will be discussed later on in
¹⁶³ this section, quarks cannot exist as free particles. They rather group to form hadronic
¹⁶⁴ matter, also known as *hadrons*. There are two kinds of hadrons; mesons and baryons.
¹⁶⁵ Mesons are quark-antiquark systems, e.g. the pion, and baryons are three-quark system,
¹⁶⁶ e.g. protons and neutrons. Quarks and anti-quarks have a baryon number of $\frac{1}{3}$ and $-\frac{1}{3}$,
¹⁶⁷ respectively.

¹⁶⁸ There are six leptons and they can be classified in charged leptons (electron e , muon
¹⁶⁹ μ , tau τ) and neutral leptons (electron neutrino ν_e , muon neutrino ν_μ , tau neutrino ν_τ).

$$\begin{pmatrix} \nu_e \\ e^- \end{pmatrix}, \quad \begin{pmatrix} \nu_\mu \\ \mu^- \end{pmatrix}, \quad \begin{pmatrix} \nu_\tau \\ \tau^- \end{pmatrix}$$

¹⁷⁰ Each lepton has a characteristic quantum number, called lepton number (L). Negatively
¹⁷¹ (positively) charged leptons have $L = -1$ ($L = 1$) and neutral leptons have $L = 0$. The
¹⁷² lepton number is conserved in all the interactions.

¹⁷³ Forces of Nature

¹⁷⁴ Forces in the SM are described by gauge theories, where the interactions is mediated by
¹⁷⁵ a vector gauge boson.

¹⁷⁶ The electromagnetic force is described by Quantum ElectroDynamics (QED) and, as
¹⁷⁷ its mediator is the photon (γ) which couples to charged particles, it only affects charged
¹⁷⁸ leptons and quarks, not neutrinos. They are instead affected by the weak force which is
¹⁷⁹ mediated by the bosons W^\pm and Z^0 .

¹⁸⁰ The weak interaction is associated with handedness (the projection of a particle spin
¹⁸¹ onto its direction of motion). Both leptons and quarks have left- and right-handed com-
¹⁸² ponents. However, only the left-handed (right-handed) component for neutrinos (anti-
¹⁸³ neutrinos) has been observed. This means that nature prefers to produce left-handed
¹⁸⁴ neutrinos and right-handed anti-neutrinos, which is the so-called parity violation.

¹⁸⁵ The strong interactions, mediated by the gluon (electrically neutral and massless), is
¹⁸⁶ described by Quantum ChromoDynamics (QCD). Its coupling increases with increasing
¹⁸⁷ distance and is smaller at short range. Moreover, due to gluon self interactions, two
¹⁸⁸ different phenomena arise; *confinement*: neither quarks nor gluons are observed as free
¹⁸⁹ particles, but only colourless “singlet” states can be observed as “jets”, namely collim-
¹⁹⁰ ated cone-shaped sprays of hadrons; *asymptotic freedom*: interactions between quarks and
¹⁹¹ gluons become weaker as the energy scale increases and the corresponding length scale
¹⁹² decreases.

¹⁹³ Table 1.1 summarises the forces described in the SM and their mediators’ main char-
¹⁹⁴ acteristics. Finally, the gravitational force, which is believed to be mediated by the grav-
¹⁹⁵ iton, is not included in Table 1.1 as it is not part of the SM.

¹⁹⁶ Symmetries and Gauge Groups

¹⁹⁷ In 1915, the mathematician Emmy Noether (23 March 1882 – 14 April 1935) proved that
¹⁹⁸ every differentiable symmetry of the action - defined as the integral over space of a Lag-

Table 1.1: Forces and mediators described by the SM

Force	Name	Symbol	Mass [GeV]	Charge
Electromagnetic	Photon	γ	0	0
Weak	W	W^\pm	80.398	$\pm e$
	Z	Z^0	91.188	0
Strong	Gluon	g	0	0

¹⁹⁹ rangian density function - of a physical system has a corresponding conservation law.
²⁰⁰ More generally, a symmetry is a property of a physical system. Under certain transforma-
²⁰¹ tions this property is preserved.

²⁰² A gauge theory in QFT, is a theory in which the Lagrangian is invariant under a con-
²⁰³ tinuous group of local transformation. Group theory was then adopted to describe the
²⁰⁴ symmetries conserved in the SM. The gauge group of the theory is the *Lie Group*. It con-
²⁰⁵ tains all the transformations between possible gauges. The Lie algebra of group generators
²⁰⁶ is therefore associated with any Lie group and for each group generator there emerges a
²⁰⁷ corresponding field: the gauge field. The quanta of the gauge fields are called *gauge bo-*
²⁰⁸ *sons*.

²⁰⁹ The three SM interactions can therefore be mathematically described by the following:

$$U(1)_Y \otimes SU(2)_L \otimes SU(3)_C \quad (1.1)$$

²¹⁰ Here, Y is the weak hypercharge, used to estimate the correlation between the electric
²¹¹ charge (Q) and the third component of the weak isospin (I_3) via the relation $Q = I_3 + Y/2$,
²¹² where I_3 can either be $\pm 1/2$ or 0 for left-handed and right-handed particles, respectively;
²¹³ C the colour charge and L the left-handedness.

²¹⁴ As of today, we can describe three of the four forces of nature with group theory. QED
²¹⁵ is an Abelian gauge theory with $U(1)$ as symmetry group, with the electromagnetic four-
²¹⁶ potential as its gauge field and with the photon as its gauge boson [9]. The interactions
²¹⁷ between charged fermions occurs by the exchange of a massless photon.

²¹⁸ The weak interaction and the strong interactions are non-Abelian gauge theories with
²¹⁹ gauge groups $SU(2)$ and $SU(3)$, respectively. As a consequence of being non-Abelian
²²⁰ the generators commutators are non-vanishing and therefore the gauge bosons can self-
²²¹ interact. The $SU(2)$ generators of the weak interaction are the massless gauge bosons
²²² $W_\mu^{\alpha=1,\dots,3}$ and, as mentioned earlier on in this chapter, they violate the parity by acting
²²³ only on left-handed particles.

²²⁴ The gauge bosons of $SU(3)_C$ are eight massless gluons, $G_\mu^{\alpha=1,\dots,8}$. The strong interaction
²²⁵ does not distinguish left- and right-handed particles. Finally, the Quarks that interact
²²⁶ through weak interaction are mixtures of SM eigenstates as described by the CKM matrix
²²⁷ [10].

²²⁸ 1.1.1 Electroweak Symmetry Breaking and the Higgs mechanism

²²⁹ In 1979 Sheldon Glashow, Abdus Salam, and Steven Weinberg were awarded the Nobel
²³⁰ Prize in Physics for their contributions to the so-called electroweak unification. In
²³¹ the mathematical description of the SM in 1.1 the electroweak interaction is described by
²³² $U(1)_Y \otimes SU(2)_L$. The electroweak physical bosons W , Z and γ are related to the four
²³³ unphysical gauge bosons $W_\mu^{\alpha=1,\dots,3}$ and B_μ^0 . In particular, to obtain the physical bosons
²³⁴ the gauge bosons have to mix as follows:

$$\begin{pmatrix} A_\mu \\ Z_\mu \end{pmatrix} = \begin{pmatrix} \cos \theta_W & \sin \theta_W \\ -\sin \theta_W & \cos \theta_W \end{pmatrix} \begin{pmatrix} B_\mu \\ W_\mu^3 \end{pmatrix} \quad (1.2)$$

²³⁵ Here, θ_W is the so-called *Weinberg angle* which is the angle by which spontaneous sym-
²³⁶ metry breaking rotates the original W_μ^3 and B_μ , producing the physical Z , and the photon.
²³⁷ θ_W can be experimentally determined in terms of the coupling strengths of the $B_\mu(g_1)$ and
²³⁸ the $W_\mu^\alpha(g_2)$ to the fermions using the relation $\tan \theta_W = g_1/g_2$. The field mixing of gauge
²³⁹ bosons that gives birth to the physical ones can be mathematically expressed by the fol-
²⁴⁰ lowing:

$$A_\mu = W_\mu^3 \sin \theta_W + B_\mu \cos \theta_W \quad (1.3)$$

²⁴¹

$$Z_\mu = W_\mu^3 \cos \theta_W - B_\mu \sin \theta_W \quad (1.4)$$

²⁴² where A_μ and Z_μ represent the photon and the Z boson, respectively. The charged vector
²⁴³ bosons, W_μ^\mp , and its complex conjugate are defined as:

$$W_\mu^\pm = \frac{1}{\sqrt{2}} (W_\mu^1 \mp iW_\mu^2) \quad (1.5)$$

²⁴⁴ Mass terms for both gauge bosons and fermionic fields are not invariant under gauge
²⁴⁵ transformations and are therefore forbidden by the electroweak gauge. Nonetheless, it is
²⁴⁶ proven by experiments that W and Z are massive [9], therefore the SM assumption only
²⁴⁷ holds if the electroweak symmetry is broken.

²⁴⁸ The SM Lagrangian can be written as the sum of the various Lagrangians describing
²⁴⁹ the three interactions and the masses of the elementary particles as follows:

$$\mathcal{L}_{\text{SM}} = \mathcal{L}_{\text{EWK}} + \mathcal{L}_{\text{QCD}} + \mathcal{L}_{\text{Mass}} \quad (1.6)$$

²⁵⁰ In order for the SM Lagrangian to remain a renormalisable theory, mass terms ($\mathcal{L}_{\text{Mass}}$)
²⁵¹ cannot be inserted by hand. A mechanism, that can preserve the gauge symmetry in
²⁵² the SM and, that can solve the inconsistency arisen from the mass difference between
²⁵³ the gauge bosons and the physical ones, is needed. A British theoretical physicist, Peter
²⁵⁴ Higgs (29 May 1929, Newcastle upon Tyne, UK), came up with a brilliant solution for
²⁵⁵ which he was awarded the 2013 Physics Nobel Prize. In the 1960s, Higgs proposed that
²⁵⁶ broken symmetry in electroweak theory could explain the origin of masses of elementary
²⁵⁷ particles, and in particular of W and Z bosons: the Higgs mechanism was given birth.
²⁵⁸ The mechanism introduces a scalar field, known as the Higgs field, thought to couple to
²⁵⁹ both massive fermions and bosons.

²⁶⁰ In the SM the Higgs field is a doublet in $SU(2)$:

$$\phi = \begin{pmatrix} \phi^+ \\ \phi^0 \end{pmatrix} \quad (1.7)$$

²⁶¹ with ϕ^+ and ϕ^0 being generic complex fields:

$$\phi^+ = \frac{\phi_1 + i\phi_2}{\sqrt{2}}, \quad \phi^0 = \frac{\phi_3 + i\phi_4}{\sqrt{2}} \quad (1.8)$$

²⁶² Consider a Lagrangian of the form:

$$\mathcal{L}_{\text{Higgs}} = (\partial_\mu \phi)^* (\partial^\mu \phi) - V(\phi) \quad (1.9)$$

²⁶³ Renormalizability and $SU(2)_L \otimes U(1)_Y$ invariance require the Higgs potential to be of the
²⁶⁴ following form:

$$V(\phi) = \mu^2 \phi^\dagger \phi + \lambda (\phi^\dagger \phi)^2 \quad (1.10)$$

²⁶⁵ Eq. 1.9 is the Higgs Lagrangian if ϕ is chosen to be the following:

$$\phi = \begin{pmatrix} \phi^+ \\ \phi^0 \end{pmatrix} = \begin{pmatrix} G^+ \\ \frac{1}{\sqrt{2}}(v + H + iG^0) \end{pmatrix}$$

266 Here, the complex scalar field G^\pm and the real scalar field G^0 correspond to Goldstone
 267 bosons, and the real scalar field H is the SM Higgs boson field [11]. These massless scalars
 268 are absorbed due to the gauge transformations by the electroweak gauge bosons of the SM:

$$\phi = \begin{pmatrix} \phi^+ \\ \phi^0 \end{pmatrix} = \begin{pmatrix} 0 \\ \frac{1}{\sqrt{2}}(v + H) \end{pmatrix} \quad (1.11)$$

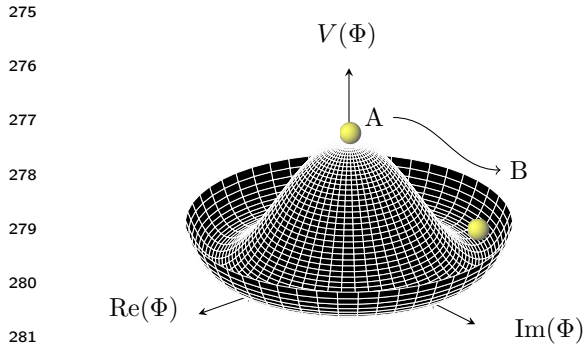
269 The Higgs potential in Eq. 1.10 is displayed in Fig. 1.1 if λ and μ are chosen to be
 270 real. Such potential has a non-zero ground state, v , also known as *vacuum expectation*
 271 *value* (VEV):

$$\phi_0 = \begin{pmatrix} 0 \\ \frac{1}{\sqrt{2}}v \end{pmatrix} \quad (1.12)$$

272 Such representation remains invariant under $U(1)$ allowing electric charge conservation.
 273 However, the SM gauge symmetry 1.1 is broken into $SU(2)_L \otimes U(1)_Y$.

274

In summary, to generate particle masses
 gauge symmetry must be broken. However,
 in order for the theory to remain
 renormalisable, the global Lagrangian
 symmetry must be preserved. This can be
 solved introducing the concept of *spontane-*
ous symmetry breaking (SSB): a mechani-
 sm that allows a symmetric Lagrangian,
 but not a symmetric VEV. In particular,



283 Figure 1.1: The Higgs potential in the complex plane.

284 given a Lagrangian invariant under a cer-
 tain transformation, T_X and a generic set
 285 of states, that transform under T_X as the elements of a multiplet, the symmetry is spon-
 286 taneously broken if one of those states is arbitrarily chosen as the ground state of the sys-
 287 tem. The interaction of the Higgs field with the $SU(2) \otimes U(1)$ gauge fields, $W_\mu^\alpha = 1, 2, 3$,
 288 result in the three gauge bosons fields acquiring mass whilst the B_0 field stays massless.

289 1.1.2 Flaws of the Standard Model

290 During Run 1 and 2 of the LHC, the SM has been extensively validated, as shown in Fig.
 291 1.2: the agreement, between the measured production cross-section of various SM pro-
 292 cesses and the SM predictions, looks very good. However, the reasons behind the mass

difference between the three generations of fermions are still not explained by the SM because masses are treated as free parameters of the theory. In addition, there are some fundamental questions that have still no answer and they will be briefly discussed this section.

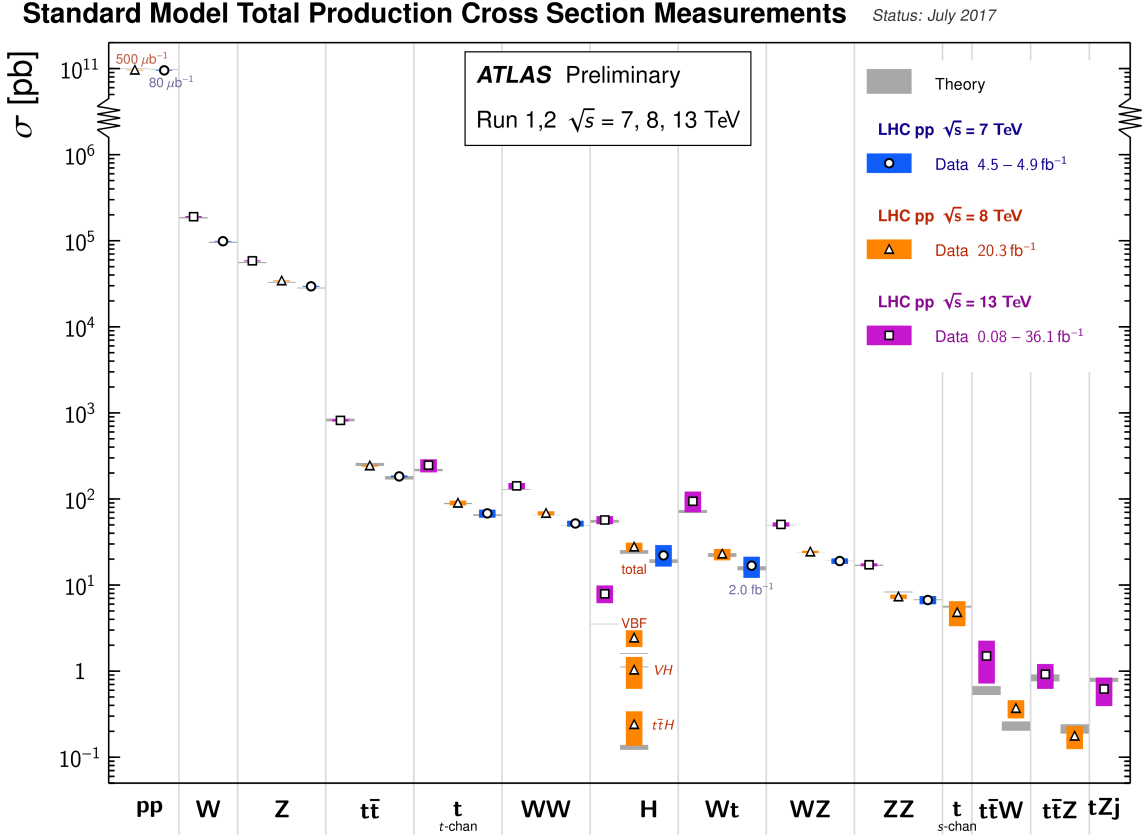


Figure 1.2: Summary of several Standard Model total production cross-section measurements, corrected for leptonic branching fractions, compared to the corresponding theoretical expectations. All theoretical expectations were calculated at NLO or higher. The luminosity used for each measurement is indicated close to the data point. Uncertainties for the theoretical predictions are quoted from the original ATLAS papers. They were not always evaluated using the same prescriptions for PDFs and scales. Not all measurements are statistically significant yet [1].

297 Hierarchy Problem

298 Due to the coupling of the Higgs field to the fermionic fields the one-loop corrections to
299 the Higgs mass receive several contributions. In particular:

$$\Delta m_H^2 = -\frac{|\lambda_f|^2}{8\pi^2} \Lambda_{\text{UV}}^2 + \dots \quad (1.13)$$

300 here, λ_f is the coupling constant to the fermionic field; Δm_H^2 is the difference between
301 the observed Higgs mass m_H^2 and the bare mass, m_H^0 (Lagrangian parameter); Λ_{UV} is

302 the ultraviolet momentum cut-off, selected to be at the Planck scale ($\sim 2 \cdot 10^{18}$ GeV), at
 303 which a QFT description of gravity is believed to become possible. The correction to the
 304 Higgs mass then, will be around 30 orders of magnitude larger than Higgs mass itself,
 305 in opposition to what has been measured. This difference just mentioned, between the
 306 electroweak scale and the Planck scale arisen from the quantum corrections to the Higgs
 307 mass, is the so-called Hierarchy Problem [12].

308 Neutrino Masses

309 The Super-Kamiokande Collaboration first, in 1998 [13], and SNO Collaboration later, in
 310 2001 [14], have provided measurements of the neutrino flux from solar and atmospheric
 311 sources. The Nobel Prize in Physics 2015 was awarded jointly to Takaaki Kajita and Arthur
 312 B. McDonald “for the discovery of neutrino oscillations, which shows that neutrinos have
 313 mass” [15]. Such feature contradicts the absence of a mechanism for mass generation for
 314 the neutrinos.

315 Various exotic solutions are on the market: one possible solution could be to add the
 316 so-called Majorana mass terms for the neutrino (seesaw mechanism). Neutrino physics
 317 could unveil physics beyond the SM.

318 Dark Matter

319 Although dark matter (DM) has never been directly observed, its existence is inferred
 320 from its gravitational effects. For example, looking at galaxies rotation, it was observed
 321 that the rotation speed was higher than expected, given the amount of visible matter. Two
 322 different reasoning arose during the last century to justify such effect either there is matter
 323 that cannot be seen by us (in terms of visible light), which contributes to the galactic mass;
 324 or the general relativity works differently at galactic distances. The former is believed to
 325 be the most likely and it implies the existence of new particles which do not interact via
 326 electromagnetic interaction, the so-called Weakly Interacting Massive Particles (WIMPs).

327 1.2 Supersymmetry

328 Supersymmetry links gravity with the other fundamental forces of nature by introducing
 329 a space-time symmetry that relates bosons to fermions and vice-versa, via a transforma-
 330 tion of the form of:

$$Q |\text{fermion}\rangle = |\text{boson}\rangle, \quad Q |\text{boson}\rangle = |\text{fermion}\rangle \quad (1.14)$$

³³¹ For each SM particle there exists a superpartner with a spin difference of $\Delta s = 1/2$. As of
³³² today, superpartners, generally called *sparticles* (where the *s* stands for “scalar”), have not
³³³ been observed yet, resulting in the assumption that SUSY must be a broken symmetry,
³³⁴ otherwise superpartners would have the same quantum numbers and masses as their
³³⁵ SM equivalent. However, if sparticles were to be too heavy (close to the Planck scale),
³³⁶ the hierarchy problem would still remain unsolved. The *soft* SUSY breaking mechanism
³³⁷ overcomes this problem imposing contrains on the masses of sparticles to a range that can
³³⁸ be experimentally explored.

³³⁹ In this section an overview of Supersymmetry (SUSY) will be presented, together with
³⁴⁰ the motivations behind the success of such theory. Finally, third-generation SUSY will be
³⁴¹ discussed as it is the most relevant theoretical support to the analyses presented in this
³⁴² work.

³⁴³ 1.2.1 Why SUSY?

³⁴⁴ One of the main motivations for SUSY is the cancellation of quadratic divergences to
³⁴⁵ Δm_H^2 . The introduction of SUSY particles with a half-integer spin difference with re-
³⁴⁶ spect to their SM provides a solution to the hierarchy problem. The Higgs mass squared
³⁴⁷ potential receives corrections from a new scalar of mass m_S of the form:

$$\Delta m_H^2 = -\frac{|\lambda_S|^2}{16\pi^2} \left[\Lambda_{UV}^2 - 2m_S^2 \ln(\Lambda_{UV}/m_S) + \dots \right] \quad (1.15)$$

³⁴⁸ where, λ_S is the coupling of SUSY particles to the Higgs field. This term cancels the
³⁴⁹ fermionic contributions in Eq. 1.13 since the couplings are the same. The experimental
³⁵⁰ value of Higgs mass will then not need any fine tuning.

³⁵¹ Fig. 1.3 shows the inverse couplings as a function of the scale for both SM and the
³⁵² Minimal Supersymmetric Standard Model (MSSM), which will be soon discussed. In the
³⁵³ SM the three lines, representing electromagnetic (dashed blue), weak (dashed red) and
³⁵⁴ strong (solid green) interactions respectively, do not meet at one point, but with the in-
³⁵⁵ troduction of supersymmetry, and assuming that the supersymmetric particles are not
³⁵⁶ heavier than about 1 TeV, they do meet. This is an indication that supersymmetry could
³⁵⁷ be discovered at the LHC. The possible unification of the coupling constants at the Planck
³⁵⁸ scale is therefore another good motivation for SUSY searches.

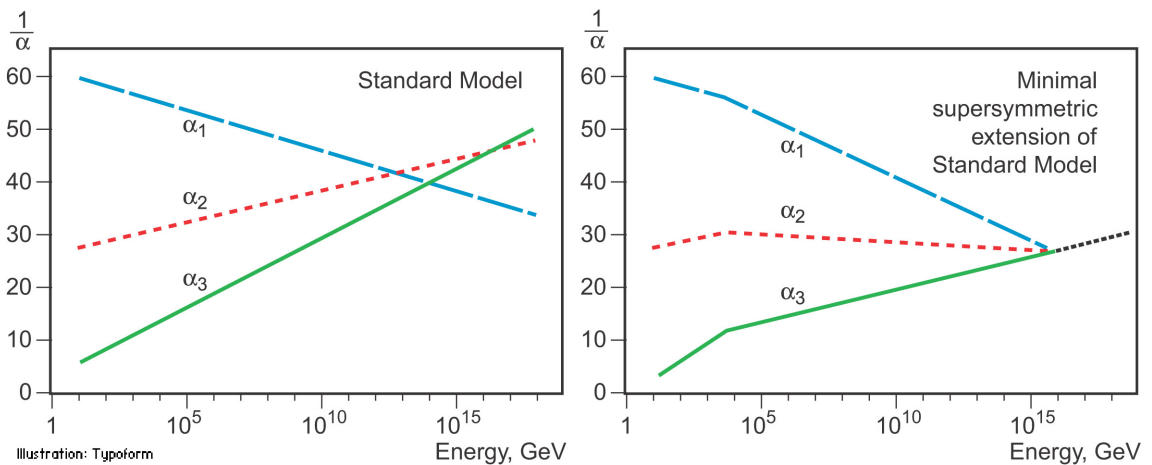


Figure 1.3: The inverse couplings of electromagnetic (dashed blue), weak (dashed red) and strong (solid green) interactions with the SM (left) and a supersymmetric model (right). In the SM the three lines do not meet at one point, but with the introduction of supersymmetry, and assuming that the supersymmetric particles are not heavier than about 1 TeV, they do meet. This is an indication that supersymmetry could be discovered at the LHC.

359 1.2.2 Minimal Supersymmetric Standard Model

360 There does not exist a unique extension of a supersymmetric Standard Model, i.e. SUSY
 361 is not a well-defined model but it is more a framework within which various SM exten-
 362 sions can be derived. The Minimal Supersymmetric Standard Model (MSSM), a minimal
 363 supersymmetric extension of the SM [16], is defined by essentially doubling up the num-
 364 ber of particles in the SM theory in order to include all the SM particles as well as their
 365 corresponding superpartners.

366 Soft SUSY breaking

367 The mass spectrum of the SUSY particles must sit somewhere at a larger scale than the SM
 368 one, as supersymmetric particles have not been discovered at the mass scale of their SM
 369 partners. This gives us a hint that supersymmetry cannot be an exact symmetry, there has
 370 to be an analogous to the electroweak symmetry breaking discussed in 1.1.1 that breaks
 371 SUSY. In particular, this must be soft or spontaneous such that broken supersymmetry still
 372 provides a solution to the hierarchy problem. This means that some new higher energy
 373 scale particles and interactions have to be added to the MSSM, but it also means that
 374 terms, containing only masses and couplings with positive mass dimension, being gauge
 375 invariant and violating SUSY, have to be added to the Lagrangian which will then be

³⁷⁶ defined as;

$$\mathcal{L} = \mathcal{L}_{\text{SUSY}} + \mathcal{L}_{\text{soft}} \quad (1.16)$$

³⁷⁷ Here, $\mathcal{L}_{\text{SUSY}}$ contains the original SUSY invariant interaction and $\mathcal{L}_{\text{soft}}$ contains all the
³⁷⁸ additional terms. A set of around 100 parameters - depending on the method - are then
³⁷⁹ introduced into the theory.

³⁸⁰ A large amount of theoretical effort has been spent trying to understand the mechani-
³⁸¹ sm for soft SUSY breaking in order to produce the desired superpartner masses and inter-
³⁸² actions properties. Among these three most studied mechanisms are; Gravity-mediated
³⁸³ supersymmetry breaking, also known as mSUGRA (minimal supergravity), which com-
³⁸⁴ municates supersymmetry breaking to the supersymmetric Standard Model through grav-
³⁸⁵ itational interactions [17]; Gauge-mediated supersymmetry breaking (GMSB) which com-
³⁸⁶ municates supersymmetry breaking to the supersymmetric Standard Model through the
³⁸⁷ Standard Model's gauge interactions [18]; Anomaly-mediated supersymmetry breaking
³⁸⁸ (AMSB), a special type of gravity-mediated supersymmetry breaking, that communicates
³⁸⁹ supersymmetry breaking to the supersymmetric Standard Model through the conformal
³⁹⁰ anomaly [19, 20]. However, such models will not be discussed any further.

³⁹¹ MSSM mass spectrum

³⁹² As for gauge bosons and the Higgs, there exists MSSM fermionic superpartner. These are
³⁹³ referred to as *Gauginos* and *Higgsinos* and, differently from the SM, in the MSSM there are
³⁹⁴ two complex Higgs doublets:

$$H_u = (H_u^+, H_u^0) \quad H_d = (H_d^0, H_d^-)$$

³⁹⁵ with their respective VEVs, v_d , v_u which are constrained by the SM Higgs VEV:

$$v = \sqrt{v_u^2 + v_d^2}$$

³⁹⁶ As per SM gauge bosons, the gaugino masses are affected by electroweak symmetry
³⁹⁷ breaking. The new mass terms, introduced in the $\mathcal{L}_{\text{soft}}$, mix to form the mass eigenstates
³⁹⁸ of the sparticles. Neutral Winos, \tilde{W}^0 , Binos, \tilde{B}^0 and higgsinos \tilde{H}^0 mix to form the four

³⁹⁹ neutralinos $\tilde{\chi}_i^0$ ($i = 1, 2, 3, 4$) as it follows;

$$\begin{pmatrix} \tilde{\chi}_1^0 \\ \tilde{\chi}_2^0 \\ \tilde{\chi}_3^0 \\ \tilde{\chi}_4^0 \end{pmatrix} = \begin{pmatrix} M_1 & 0 & -c_\beta s_W m_Z & c_W s_\beta m_Z \\ 0 & M_2 & c_\beta c_W m_Z & -c_W s_\beta m_Z \\ -c_\beta s_W m_Z & c_\beta s_W m_Z & 0 & -\mu \\ s_\beta c_W m_Z & -s_\beta c_W m_Z & -\mu & 0 \end{pmatrix} \begin{pmatrix} \tilde{B}^0 \\ \tilde{W}^0 \\ \tilde{H}_u^0 \\ \tilde{H}_d^0 \end{pmatrix} \quad (1.17)$$

⁴⁰⁰ Here, $c_\beta = \cos \beta$, $(s_\beta) = \sin \beta$, $c_W = \cos \theta_W$ and $(s_W) = \sin \theta_W$. M_1 , M_2 are related to gaugino masses and μ to higgsino mass, β is the ratio of the electroweak coupling constants and θ_W is the ratio of the VEVs of the two Higgs doublet fields, and finally, m_Z (m_W) is the mass of the Z (W) boson. The neutralino indeces are conventionally assumed to increase with their masses.

⁴⁰⁵ The charged winos \tilde{W}^\pm and higgsinos \tilde{H}^\pm mix to form four *charginos*, $\tilde{\chi}_i^\pm$ ($i = 1, 2$) as it follows;

$$\begin{pmatrix} \tilde{\chi}_1^\pm \\ \tilde{\chi}_2^\pm \end{pmatrix} = \begin{pmatrix} M_2 & \sqrt{2}m_W \sin \beta \\ \sqrt{2}m_W \cos \beta & \mu \end{pmatrix} \begin{pmatrix} \tilde{W}^\pm \\ \tilde{H}^\pm \end{pmatrix} \quad (1.18)$$

⁴⁰⁷ Charginos and neutralinos, given birth by the mixing described in Eq. 1.18 and 1.17, will be referred to as bino-like, wino-like or higgsino-like depending on their phenomenology. Gluinos do not mix as they carry colour charge, and its mass is linked to M_3 .

⁴¹⁰ Sleptons and squarks states also mix due to electroweak symmetry breaking, although it is assumed to be zero except for the third-generation particles. Stop, \tilde{t}_L , \tilde{t}_R , sbottom \tilde{b}_L , \tilde{b}_R , and stau, $\tilde{\tau}_L$, $\tilde{\tau}_R$ mix to give mass eigenstates, \tilde{t}_1 , \tilde{t}_2 , \tilde{b}_1 , \tilde{b}_2 , $\tilde{\tau}_1$, $\tilde{\tau}_2$, respectively. As with the neutralinos and charginos, the convention is to refer to the one with the lower index as the lighter one. Finally, the Higgs sector is also affected. There are five mass eigenstates, h^0 , H^0 , A^0 , and H^\pm . These, together with the other MSSM particles are listed in Table 1.2.

⁴¹⁶ 1.2.3 Supersymmetry Phenomenology

⁴¹⁷ As mentioned earlier on in this chapter, the introduction of SUSY particles overcomes the problem of an unnatural fine-tuning to the Higgs mass due to its quadratic corrections, given that the stops have masses typically around 1 TeV.

⁴²⁰ R-parity

⁴²¹ The most general MSSM can contain operators that violate baryon and / or lepton number, thus allowing proton decays. The non-observation of proton decays forbids the existence

Table 1.2: SUSY particles in the MSSM

Name	Spin	Gauge Eigenstates	Mass Eigenstates
Squarks (\tilde{q})	0	$\tilde{u}_L \tilde{u}_R \tilde{d}_L \tilde{d}_R$	(same)
		$\tilde{c}_L \tilde{c}_R \tilde{s}_L \tilde{s}_R$	(same)
		$\tilde{t}_L \tilde{t}_R \tilde{b}_L \tilde{b}_R$	$\tilde{t}_1 \tilde{t}_2 \tilde{b}_1 \tilde{b}_2$
Sleptons (\tilde{l})	0	$\tilde{e}_L \tilde{e}_R \tilde{\nu}_L$	(same)
		$\tilde{\mu}_L \tilde{\mu}_R \tilde{\nu}_L$	(same)
		$\tilde{\tau}_L \tilde{\tau}_R \tilde{\nu}_{\tau}$	$\tilde{\tau}_1 \tilde{\tau}_2 \tilde{\nu}_{\tau}$
Higgs bosons	0	$H_u^0 H_d^0 H_u^+ H_d^-$	$h^0 H^0 A^0 H^{\pm}$
Neutralinos ($\tilde{\chi}_j^0$)	1/2	$\tilde{B}^0 \tilde{W}^0 \tilde{H}_u^0 \tilde{H}_d^0$	$\tilde{\chi}_1^0 \tilde{\chi}_2^0 \tilde{\chi}_3^0 \tilde{\chi}_4^0$
Charginos ($\tilde{\chi}_i^{\pm}$)	1/2	$\tilde{W}^{\pm} \tilde{H}_u^{\pm} \tilde{H}_d^{\mp}$	$\tilde{\chi}_1^{\pm} \tilde{\chi}_2^{\pm}$
Gluino	1/2	\tilde{g}	(same)
Gravitino	3/2	\tilde{G}	(same)

⁴²³ of such terms. A possibility to avoid these operators is to introduce a new discrete symmetry named R -parity. The conserved quantum number is defined as;

$$P_R = (-1)^{3(B-L)+2s} \quad (1.19)$$

⁴²⁵ where B , L , and s are the baryon, lepton, and spin number, respectively.

⁴²⁶ If a certain SUSY model is R -parity conserving, then the SM particles have $R = 1$
⁴²⁷ and SUSY partners have $R = -1$. When R -parity conservation is imposed on MSSM
⁴²⁸ models, the mixing between particles and sparticles cannot occur, resulting in the number
⁴²⁹ of SUSY particles to be even at every interaction vertex. Furthermore, all sparticles must
⁴³⁰ be pair-produced and the Lightest Supersymmetric Particle (LSP) has to be stable and can
⁴³¹ therefore be a good Dark Matter candidate.

⁴³² Although the SUSY searches in a R -parity violating (RPV) scenario have been ex-
⁴³³ tensively investigated by the particle-physics community, in this work only R -parity con-
⁴³⁴ serving (RPC) models, where the $\tilde{\chi}_1^0$ is assumed to be the LSP, were considered.

⁴³⁵ Phenomenological MSSM (pMSSM)

⁴³⁶ In 1.2.2 it was mentioned that, once the SUSY soft breaking occurred, the unconstrained
⁴³⁷ MSSM has more than 100 parameters in addition to the Standard Model ones. However,
⁴³⁸ this makes the SUSY searches, i. e. the phenomenological analyses, (e. g. finding regions,

⁴³⁹ in parameter space, that are consistent with the data) rather impractical. Under the fol-
⁴⁴⁰ lowing three assumptions;

- ⁴⁴¹ • no new source of CP-violation (CKM matrix is the only source)
- ⁴⁴² • no Flavour Changing Neutral Currents
- ⁴⁴³ • first- and second-generation universality

⁴⁴⁴ such number can be reduced down to 19. The introduction of such parameters, sum-
⁴⁴⁵ marised in Table 1.3, defines the so-called phenomenological MSSM (pMSSM).

Table 1.3: Parameters in the pMSSM.

Parameter	Description	N. of parameters
M_1, M_2, M_3	Bino, Wino and gluino masses	3
M_A	pseudoscalar Higgs boson mass	1
μ	higgsino mass	1
$m_{\tilde{q}}, m_{\tilde{u}_R}, m_{\tilde{d}_R},$ $m_{\tilde{Q}_L}, m_{\tilde{t}}, m_{\tilde{b}}$	first- and second-generation squark masses third generation squark masses	3 3
$m_{\tilde{l}}, m_{\tilde{e}_R}$	first- and second-generation slepton masses	2
$m_{\tilde{\tau}_R}$	third-generation slepton masses	2
A_t, A_b, A_τ	third-generation trilinear couplings	3
$\tan \beta$	two-higgs-doublet fields VEVs ratio	1

⁴⁴⁶ Such parameter space is still rather large and it makes pMSSM searches extremely chal-
⁴⁴⁷ lenging and difficult to exclude. To overcome this problem *simplified models* are introduced.
⁴⁴⁸ In other words, a certain signal process is extracted from the model and only particles
⁴⁴⁹ contributing to a certain decay mode will be considered, e. g. $\tilde{t}_1 \rightarrow t + \tilde{\chi}_1^0$ only targets the
⁴⁵⁰ 2-body decay ignoring the remaining SUSY mass spectrum. The number of parameters
⁴⁵¹ will then boil down to 2; $m_{\tilde{t}}$ and $m_{\tilde{\chi}_1^0}$, allowing the reinterpretation of the results and
⁴⁵² providing a powerful tool to constrain various models.

⁴⁵³ In this work only analyses laying their theoretical assumptions on such simplified
⁴⁵⁴ models will be presented.

⁴⁵⁵ Third generation SUSY

⁴⁵⁶ Fig. 1.4 shows SUSY particles production cross-sections for squarks that do not contrib-
⁴⁵⁷ ute to gluino production diagrams and vice versa, i. e. treating squarks and gluinos as

⁴⁵⁸ *decoupled* making the cross-section of squark pair-production be the same for all families.
⁴⁵⁹ While gluinos production cross-sections are fairly large, SUSY electroweak production
⁴⁶⁰ cross-sections of neutralinos and charginos are considerably lower. Sleptons produc-
⁴⁶¹ tion cross-section, which is not displayed, would sit just below higgsino-like char-
⁴⁶² gino/neutralino production cross-section.

⁴⁶³ Due to the cross-section being around a factor of six smaller than $t\bar{t}$ production (when
⁴⁶⁴ $m_{\tilde{t}_1} \sim m_t$), third-generation SUSY analyses are very challenging. Furthermore, the cross-
⁴⁶⁵ section of such processes dramatically decreases with increasing $m_{\tilde{t}}$ (or $m_{\tilde{b}}$). Nonetheless,
⁴⁶⁶ for example, searches for direct \tilde{t}_1 production with $\tilde{t}_1 \rightarrow t + \tilde{\chi}_1^0$ are sensitive in a scenario
⁴⁶⁷ where $m_{\tilde{t}_1} \gg m_t + m_{\tilde{\chi}_1^0}$ as the large E_T^{miss} , from the neutralinos, provides discriminating
⁴⁶⁸ power for $t\bar{t}$ rejection.

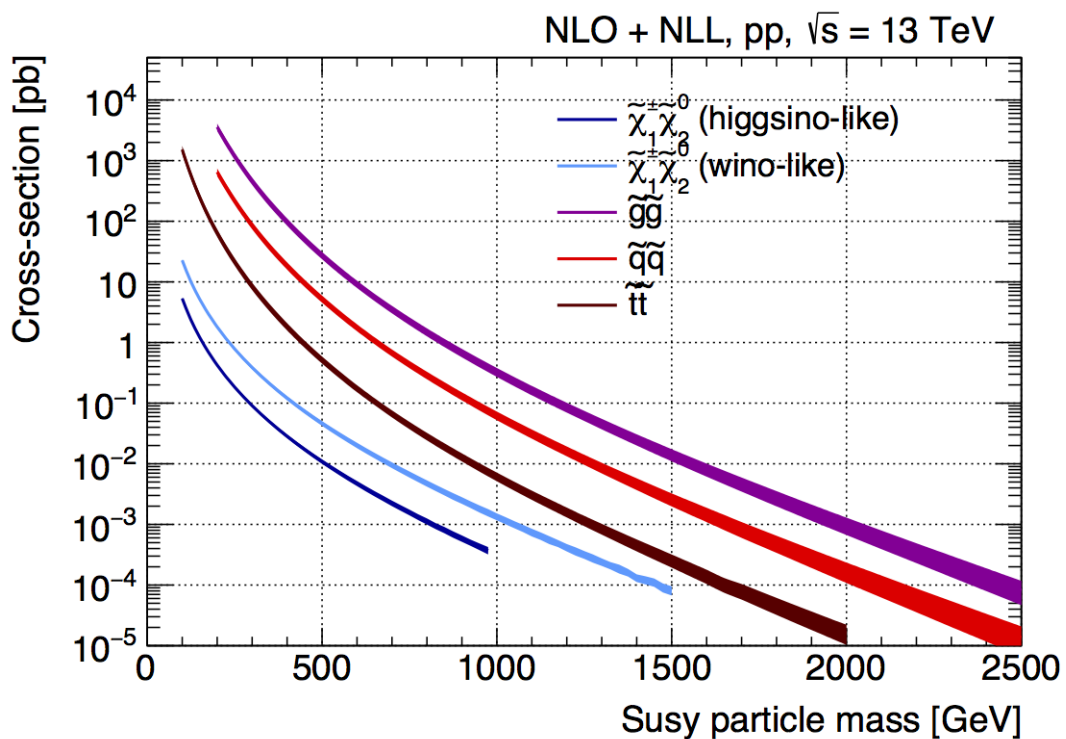


Figure 1.4: NLO+NLL production cross-sections as a function of mass at $\sqrt{s} = 13$ TeV [2]

⁴⁶⁹ There exists various decay modes of pair-produced stops, depending on the masses
⁴⁷⁰ of the decay products;

- ⁴⁷¹ • $\tilde{t} \rightarrow t \tilde{\chi}^0$
- ⁴⁷² • $\tilde{t} \rightarrow b \tilde{\chi}^\pm \rightarrow b W \tilde{\chi}^0$ (on/off-shell W) or $\tilde{t} \rightarrow b W \tilde{\chi}^0$ (off-shell top)
- ⁴⁷³ • $\tilde{t} \rightarrow c \tilde{\chi}^0$

474 • $\tilde{t} \rightarrow b f f' \tilde{\chi}^0$

475 Figure 1.5 shows a schematic representation of the parameter space $(m_{\tilde{t}_1}, m_{\tilde{\chi}_1^0})$ and the
476 different region where each of the above-mentioned process dominates. In particular,
477 $\tilde{t} \rightarrow b \tilde{\chi}^\pm$ is allowed when $m_{\tilde{\chi}^0} < m_{\tilde{\chi}^\pm} < m_{\tilde{t}} - m_b$.

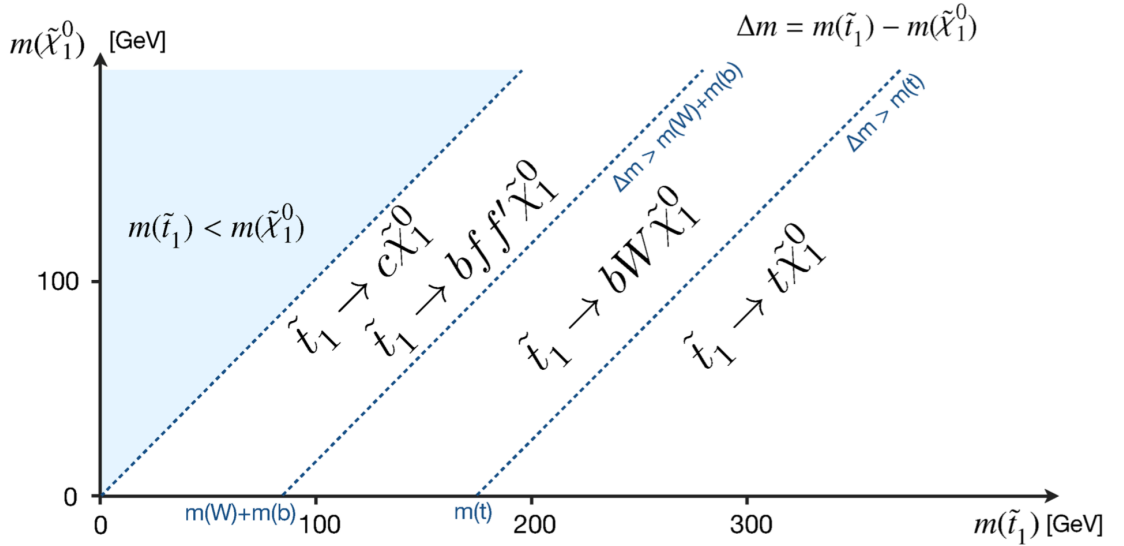


Figure 1.5: Illustration of stop decay modes in the $(m_{\tilde{t}_1}, m_{\tilde{\chi}_1^0})$ mass place where the $\tilde{\chi}_1^0$ is assumed to be the lightest supersymmetric particle. The dashed blue lines indicate thresholds separating regions where different processes dominate.

478 In the models considered in this thesis, either $\tilde{\chi}_2^0$ or $\tilde{\chi}_1^\pm$ is assumed to be the so-called
479 next lightest supersymmetric particle (NLSP). Three different decay scenarios were con-
480 sidered in this work; (a) where both top squarks decay via $\tilde{t} \rightarrow t^{(*)} \tilde{\chi}_1^0$ ¹; (b) at least one
481 of the stops decays via $\tilde{t} \rightarrow b \tilde{\chi}_1^\pm \rightarrow b W^{(*)} \tilde{\chi}_1^0$; (c) where $m_{\tilde{\chi}_2^0}$ is small enough to allow
482 one stop to decay via $\tilde{t} \rightarrow t \tilde{\chi}_2^0 \rightarrow h/Z \tilde{\chi}_1^0$. Here, h is the SM Higgs boson (125 GeV),
483 as illustrated in Figure 1.6(a)–(c), respectively. Furthermore, top squarks can also be in-
484 directly produced through the so-called gluino-mediated stop production, as shown in
485 Figure 1.6(d).

¹ The symbol (*) indicates that the decay can occur with the top quark being produced off-shell (region between the second and third dashed line in Fig. 1.5)

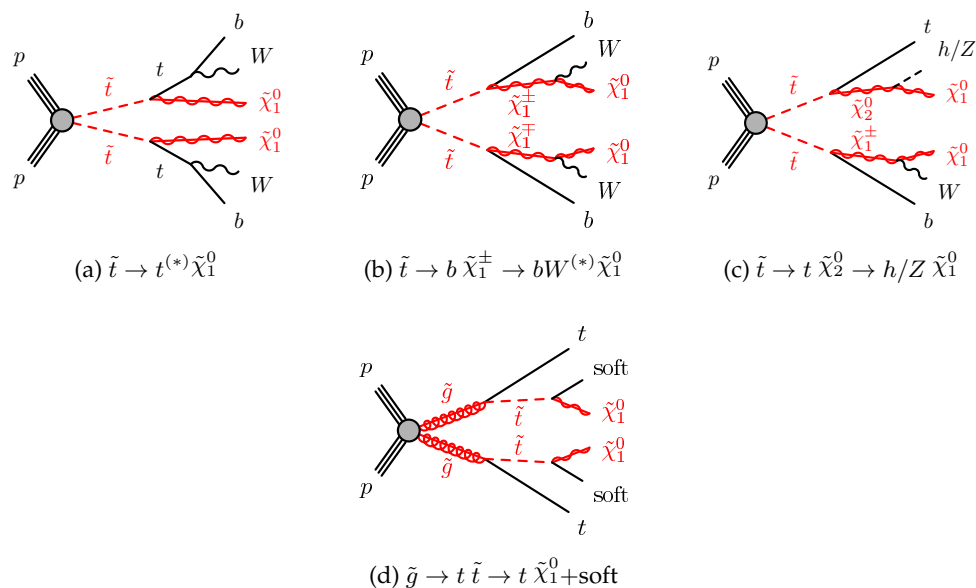


Figure 1.6: Diagrams of the decay topologies of the signal models considered in this work. The term “soft” refers to decay products that have transverse momenta below the detector thresholds.

⁴⁸⁶ 2 | The ATLAS Experiment at the ⁴⁸⁷ LHC

⁴⁸⁸

*We are rather like children, who
must take a watch to pieces to see
how it works*

Sir Ernest Rutherford

⁴⁸⁹ ATLAS (A Toroidal LHC ApparatuS) is one of the four main experiments (ATLAS,
⁴⁹⁰ CMS, ALICE, LHCb) taking data at a center-of-mass energy of 13 TeV using beams de-
⁴⁹¹ livered by the Large Hadron Collider (LHC). In this chapter an overview of the LHC will
⁴⁹² be given in Section 2.1, then the ATLAS detector will be described in Section 2.2, and fi-
⁴⁹³ nally the Trigger system, used to cleverly store the data, will be described in Section 2.3. A
⁴⁹⁴ more in-depth description of the Trigger algorithms I have been involved in will be given
⁴⁹⁵ in Chapter 3.

⁴⁹⁶ 2.1 The LHC

⁴⁹⁷ As of today, the LHC is the world's largest and most powerful particle accelerator. It was
⁴⁹⁸ designed to help answer some of the fundamental open questions in particle physics by
⁴⁹⁹ colliding protons at an unprecedented energy and luminosity. It is located at the European
⁵⁰⁰ Organisation for Nuclear Research (CERN), in the Geneva area, at a depth ranging from
⁵⁰¹ 50 to 175 metres underground. It consists of a 27-kilometre ring made of superconducting
⁵⁰² magnets, and inside it two high-energy particle beams travel in opposite directions and
⁵⁰³ in separate beam pipes.

⁵⁰⁴ The beams are guided around the ring by a strong magnetic field generated by coils -
⁵⁰⁵ made of special electric cables - that can operate in a superconducting regime. 1232 super-
⁵⁰⁶ conducting dipole and 392 quadrupole magnets, with an average magnetic field of 8.3 T,

507 are employed and kept at a temperature below 1.7 K, in order to preserve their superconducting properties. The formers are used to bend the beams and the latters to keep them
 508 focused while they get accelerated.
 509

510 The collider first went live on September 2008 even though, due to a magnet quench
 511 incident that damaged over 50 superconducting magnets, it has been operational since
 512 November 2009 when low-energy beams circulated in the tunnel for the first time since the
 513 incident. This also marked the start of the main research programme and the beginning
 514 of the so-called Run 1: first operational run (2009 - 2013).

515 Performance of the LHC

516 In June 2015 the LHC restarted delivering physics data, after a two-year break, the so-
 517 called Long Shutdown 1 (LS1), during which the magnets were upgraded to handle the
 518 current required to circulate 7-TeV beams. It was the beginning of the so-called Run 2 -
 519 second operational run (2015-2018) - during which LHC has collided up to 10^{11} bunches
 520 of protons every 25 ns at the design luminosity - the highest luminosity the detector was
 521 designed to cope with - of $2 \cdot 10^{34} \text{ cm}^{-2} \text{s}^{-1}$. The definition of the luminosity is:

$$\mathcal{L} = f \frac{n_b N_1 N_2}{4\pi\sigma_x\sigma_y} \quad (2.1)$$

522 where N_1 and N_2 are the number of protons per bunch in each of the colliding beams, f
 523 is the revolution frequency of the bunch collisions, n_b the number of proton per bunch,
 524 and σ_x and σ_y are the horizontal and vertical dimensions of the beam. The luminosity is
 525 strictly related to the number of collisions occurring during a certain experiment via the
 526 following:

$$\mathcal{N}_{\text{event}} = \mathcal{L}\sigma_{\text{event}} \quad (2.2)$$

527 where σ_{event} is the cross section of the process under investigation. It has not only collided
 528 protons but also heavy ions, in particular lead nuclei at $\sqrt{s_{NN}} = 5.02 \text{ TeV}$, at a luminosity
 529 of $10^{27} \text{ cm}^{-2} \text{s}^{-1}$ [21].

530 Acceleration stages

531 Before reaching the maximum energy, the proton beams are accelerated by smaller ac-
 532 celerators through various stages. Figure 2.1 shows a sketch of the CERN's accelerator
 533 complex. It all begins at the linear accelerator LINAC 2. Here protons are accelerated up
 534 to 50 MeV, and then injected in the Proton Synchrotron Booster (PSB) where they reach

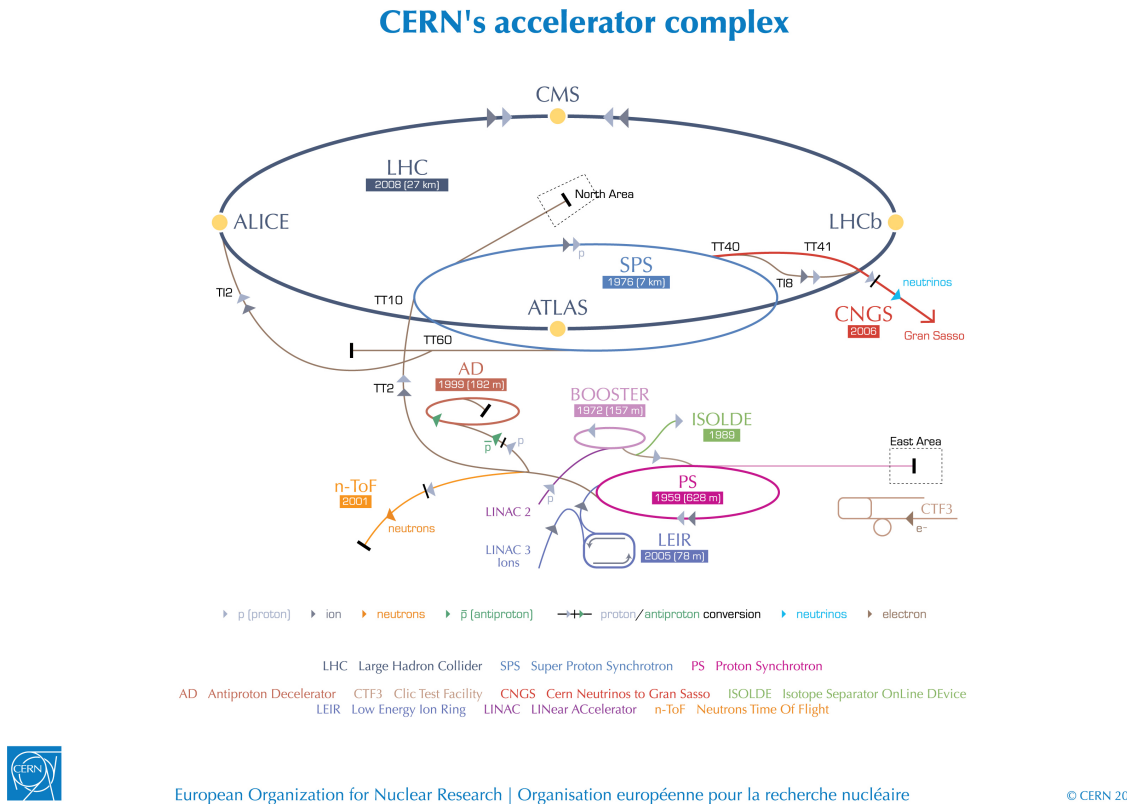


Figure 2.1: CERN Accelerator complex. The LHC is the last ring (dark grey line). Smaller machines are used for early-stage acceleration and also to provide beams for other experiments [3].

535 1.4 GeV. The next stage is the Proton Synchrotron (PS), which boosts the beams up to 25
 536 GeV and then the Super Proton Synchrotron (SPS) makes them reach energies up to 450
 537 GeV. Eventually, the beams are injected in bunches with a 25 ns spacing into the LHC,
 538 where they travel in opposite directions, while they are accelerated to up to 13 TeV. Once
 539 the bunches reach the maximum energy, they are made collide at four different points,
 540 inside four experiments around the ring [22].

541 The heavy ion beams acceleration procedure is slightly different. Their journey starts
 542 at LINAC 3 first, and the Low Energy Ion Ring (LEIR) then, before they make their way
 543 into the PS where they follow the same path as the protons [22].

544 The four large detectors on the collision points are; the multi-purpose detectors A Tor-
 545 oidal LHC ApparatuS (ATLAS), and Compact Muon Solenoid (CMS) [23], Large Hadron
 546 Collider beauty (LHCb) [24], which focuses on flavour physics, and A Large Ion Collider
 547 Experiment (ALICE) [25] which specialises in heavy ion physics. The *big four* are not the
 548 only experiments at the CERN's accelerator complex. There also are smaller experiments
 549 based at the the four caverns about the collision points e.g. TOTEM, LHCf and MoEDAL,
 550 but this will not be discussed any further in this thesis.

551 2.2 The ATLAS Detector

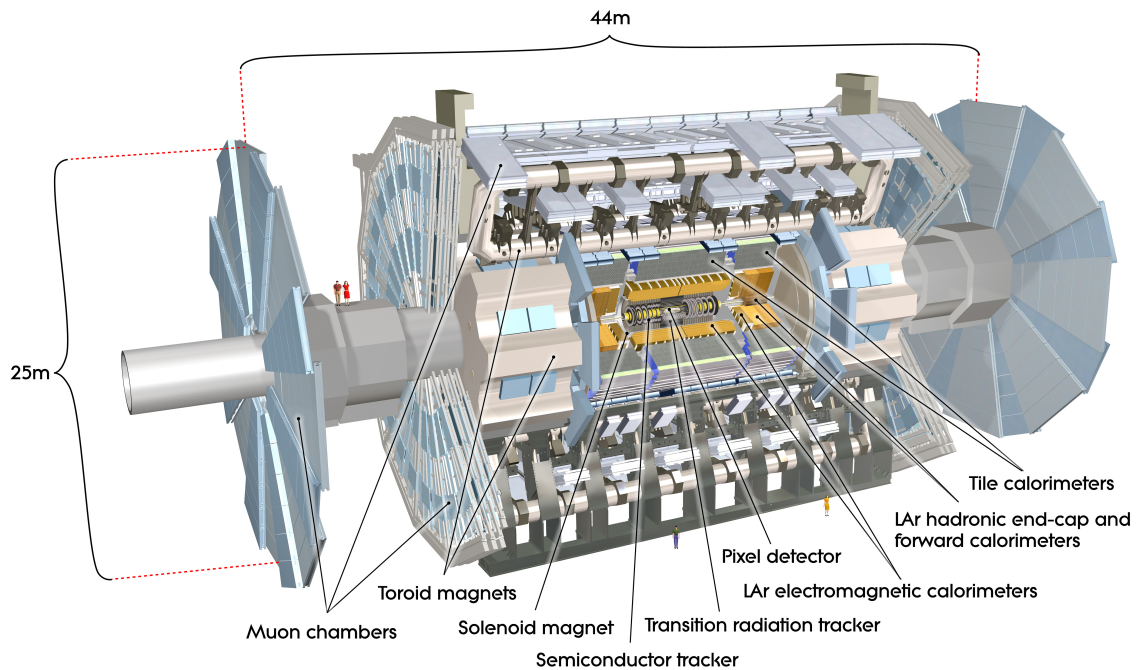


Figure 2.2: Cut-away view of the ATLAS detector. The dimensions of the detector are 25 m in height and 44 m in length. The overall weight of the detector is approximately 7000 tonnes [3].

552 ATLAS is a general-purpose detector designed to collect data with the highest luminosity provided by the LHC. It is located at CERN’s Point 1 cavern and it measures about
 553 45 m in length and 25 m in diameter. It has a forward-backward symmetric cylindrical
 554 geometry with respect to the interaction point and it is designed to reconstruct and mea-
 555 sure physics objects such as electrons, muons, photons and hadronic jets. Its design was
 556 optimised to be as sensitive as possible to the discovery of the Higgs boson and beyond-
 557 the-Standard-Model (BSM) physics. In fact, thanks to the other sub-systems, ATLAS is
 558 able to observe all possible decay products by covering nearly 4π steradians of solid angle.
 559

560 In Figure 2.2 a cut-away view of ATLAS with all its components is shown. The inner-
 561 most layer is the Inner Detector (ID) which is the core of the tracking system and consists
 562 of a Pixel, a Silicon micro-strip tracker (SCT), and a Transition Radiation Tracker (TRT).
 563 It is submerged in a 2 T magnetic field, generated by a thin superconducting solenoid,
 564 which bends all the charged particles’ trajectories allowing transverse momentum meas-
 565 urement. The electromagnetic and hadronic calorimeters form the next layer and they are
 566 both used to perform precise energy measurements of photons, electrons, and hadronic
 567 jets. Finally, the outermost layer corresponds to the Muon Spectrometer (MS) which, to-

568 gether with the ID, enclosed in a toroidal magnetic field, allows precise measurement of
 569 momentum and position of muons. These sub-detectors will be discussed in more detail
 570 in the following sections.

571 The ATLAS coordinate system

572 A coordinate system is taken on for the spatial definition of the sub-systems and kinematic
 573 measurement of physics processes. Such system is defined starting from the interaction
 574 point, defined as the origin. The z -axis is defined by the beam direction and the $x - y$
 575 plan, as transverse to the beam direction.

576 A quantity, known as pseudorapidity, (η), is defined to describe the angle of a particle
 577 coming out of the collision, with respect to the beam axis:

$$\eta \equiv -\ln(\tan(\theta/2))$$

578 Here θ is the polar angle. The azimuthal angle, ϕ , is defined around the beam axis and
 579 the polar angle. In the (η, ϕ) space a distance ΔR can be therefore defined as

$$\Delta R = \sqrt{\Delta\eta^2 + \Delta\phi^2}$$

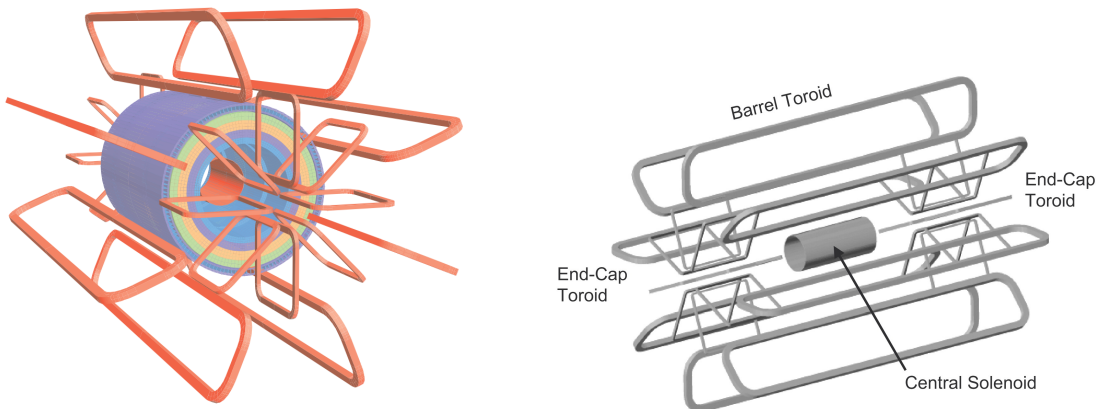
580 where $\Delta\eta$ and $\Delta\phi$ are the differences in pseudorapidity and azimuthal angle between any
 581 two considered objects. A central and a forward region of pseudorapidity are also defined
 582 such that the detector components are described as part of the *barrel* if they belong to the
 583 former or as part of the *end-caps* if they belong to the latter.

584 2.2.1 The Magnet System

585 The ATLAS magnet system, 26 m long with a 22 m diameter, generates the magnetic field
 586 needed to bend the trajectories of charged particles in order to perform momentum meas-
 587 urement. Figure 2.3a and 2.3b show the geometry of the system and its components,
 588 which are made of NbTi - superconducting material - and will be described in the follow-
 589 ing paragraphs.

590 The Central Solenoid

591 With an axial length of 5.8 m, an inner radius of 2.46 m, and an outer radius of 2.56 m, the
 592 central solenoid magnet is located between the ID and the ECAL. Its function is to bend
 593 the charged particles that go through the ID and it is aligned on the beam axis providing



(a) Geometry of magnet windings and tile calorimeter steel. The eight barrel toroid coils, with the end-cap coils interleaved are visible. The solenoid winding lies inside the calorimeter volume [4].

(b) Schematic view of the superconducting magnets [26].

Figure 2.3: The ATLAS magnet system.

594 a 2 T axial magnetic field that allows accurate momentum measurement up to 100 GeV
 595 [26].

596 **The Barrel and the End-cap Toroids**

597 Figure 2.3b displays the toroid magnetic system that surrounds the calorimeters. With its
 598 cylindrical shape this component consists of a barrel and two end-caps toroids, each with
 599 eight superconducting coils. The system allows accurate measurement of muon momenta
 600 using a magnetic field of approximately 0.5 T (barrel) for the central regions and 1 T (end-
 601 cap) for the end-cap regions, respectively, which bends the particles in the θ direction.

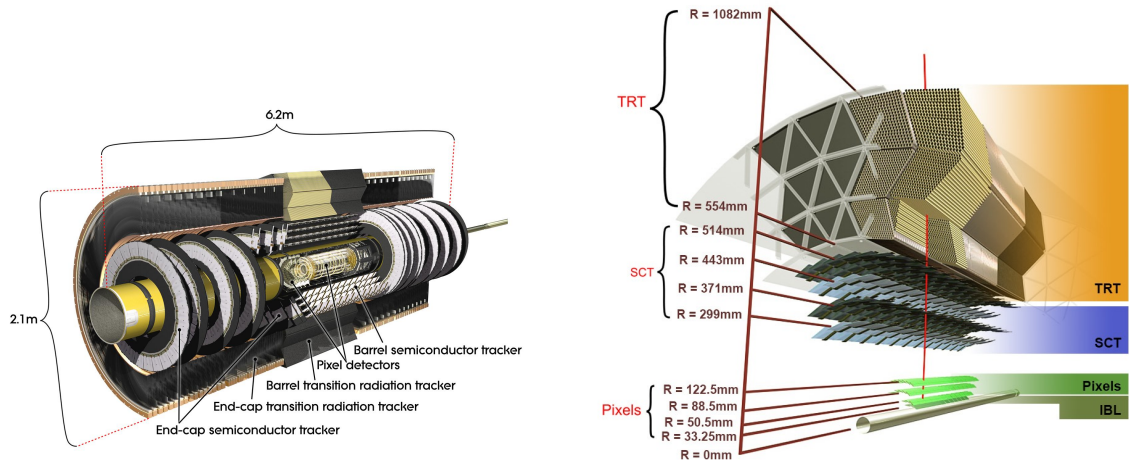
602 **2.2.2 The Inner Detector**

603 The Inner Detector (ID) [27] is the innermost component of the ATLAS detector i. e. the
 604 nearest sub-detector to the interaction region and it is used to reconstruct charged particle
 605 tracks used in the selection of physics objects. In fact, it allows robust track reconstruction,
 606 with accurate impact parameter resolution ($\sim 20\mu m$) and precise primary and secondary
 607 vertex reconstruction for charged particles (tracks) above 500 MeV and within $|\eta| < 2.5$.

608 The ID is comprised of independent and concentric sub-systems, which are all shown
 609 in Figure 2.4:

610 • Insertable B-Layer (IBL):

611 innermost Pixel Detector layer added during ATLAS Run 2 upgrade (2013/2014) to



(a) Overview of the ATLAS ID with labels and dimensions.

(b) Diagram of the ATLAS ID and its sub-detectors.

Figure 2.4: The ATLAS Inner Detector

- 612 improve vertexing and impact parameter reconstruction;
- 613 • Silicon Pixel Tracker (Pixel):
614 made of silicon pixel layers and used mainly for reconstructing both the primary
615 and secondary vertices in an event;
- 616 • SemiConductor Tracker (SCT):
617 comprised of silicon microstrip layers; thanks to its resolution ($17 \times 580 \mu\text{m}$) it can
618 accurately measure particle momenta;
- 619 • Transition Radiation Tracker (TRT):
620 final layer comprised of various layers of gaseous straw tube elements surrounded
621 by transition radiation material.

622 These sub-detectors will be discussed in the following sections.

623 IBL

624 The IBL [28] is the innermost Pixel Detector layer as shown in Figure 2.4b. It is comprised
625 of 6M channels and each pixel measures $50 \times 250 \mu\text{m}$. Its resolution is $8 \times 40 \mu\text{m}$,
626 The addition of this new layer brought a considerable improvement on the performance of the
627 Pixel Detector by enhancing the quality of impact parameter reconstruction of tracks. In
628 particular, this was achieved by improving the vertex finding efficiency and the tagging
629 of bottom-quark-initiated jets (b -jets) which, in case of a B-layer failure, can be restored
630 by the IBL. Besides these improvements, the IBL insertion allowed ATLAS to better cope

631 with high luminosity effects such as the increase in event pile-up, which leads to high
632 occupancy and read-out inefficiency.

633 Pixel

634 The Pixel detector is comprised of 1750 identical sensorchip-hybrid modules, each cover-
635 ing an active area of 16.4×60.8 mm. The total number of modules correspond to roughly
636 80 million semiconductor silicon pixels. The nominal pixel size is $50 \mu\text{m}$ in the ϕ direction
637 and $400 \mu\text{m}$ in the barrel region, along the z -axis (beam axis) [29]. The reason why such a
638 large amount of pixels is employed is justified by the need to cope with the high lumino-
639 sity in ATLAS. The silicon pixel detector measures 48.4 cm in diameter and 6.2 m in length
640 providing a pseudorapidity coverage of $|\eta| < 2.5$. Figure 2.4b shows the three concentric
641 barrel layers placed at 50.5 mm, 88.5 mm and 122.5 mm respectively. Furthermore, the
642 Pixel detector is made of six disk layers, three for each forward region, such that when a
643 charged particle crosses the layers it will generate a signal at least in three space points.
644 The fine granularity of such detector allows accurate measurement and precise vertex re-
645 construction, as it provides a more accurate position measurement as a large detection
646 area is available. In particular, it has a resolution of $10 \times 115 \mu\text{m}$.

647 SCT

648 The SCT is made of 4088 modules of silicon micro-strip detectors arranged in four con-
649 centric barrel layers. It is mainly used for precise momentum reconstruction over a range
650 $|\eta| < 2.5$ and it was designed for precision measurement of the position using four points
651 (corresponding to eight silicon layers), obtained as track hits when crossing the layers.
652 Figure 2.4b shows the structure of the SCT with its four concentric barrel layers with radii
653 ranging from 299 mm to 514 mm and two end-cap layers. Each module has an intrinsic
654 resolution of $17 \mu\text{m}$ in the $R - \phi$ direction and $580 \mu\text{m}$ in the z direction. As the SCT is fur-
655 ther away from the beam-pipe than the Pixel detector, it has to cope with reduced particle
656 density. This allows for reduced granularity maintaining the same level of performance of
657 the Pixel detector: SCT can use ~ 6.3 million read-out channels.

658 TRT

659 The last and outermost of the sub-systems in the ID is the TRT. It is a gaseous detector
660 which consists of 4 mm diameter straw tubes wound from a multilayer film reinforced
661 with carbon fibers and containing a $30 \mu\text{m}$ gold plated tungsten wire in the center. The

straw is filled with a gas mixture of 70% Xe, 27% CO₂ and 3% O₂ [30]. As shown in Figure 2.4b, its section consists of three concentric layers with radii ranging from 544 mm to 1082 mm, each of which has 32 modules containing approximately 50,000 straws, 1.44 m in length, aligned parallel to the beam direction with independent read-out at both ends. Both end-cap sections are divided into 14 wheels, with roughly 320,000 straws in the R-direction. The average 36 hits per track in the central region of the TRT allow continuous tracking to enhance pattern recognition and momentum resolution in the $|\eta| < 2.5$ region. It also improves the p_T resolution for longer tracks.

2.2.3 The Calorimeters

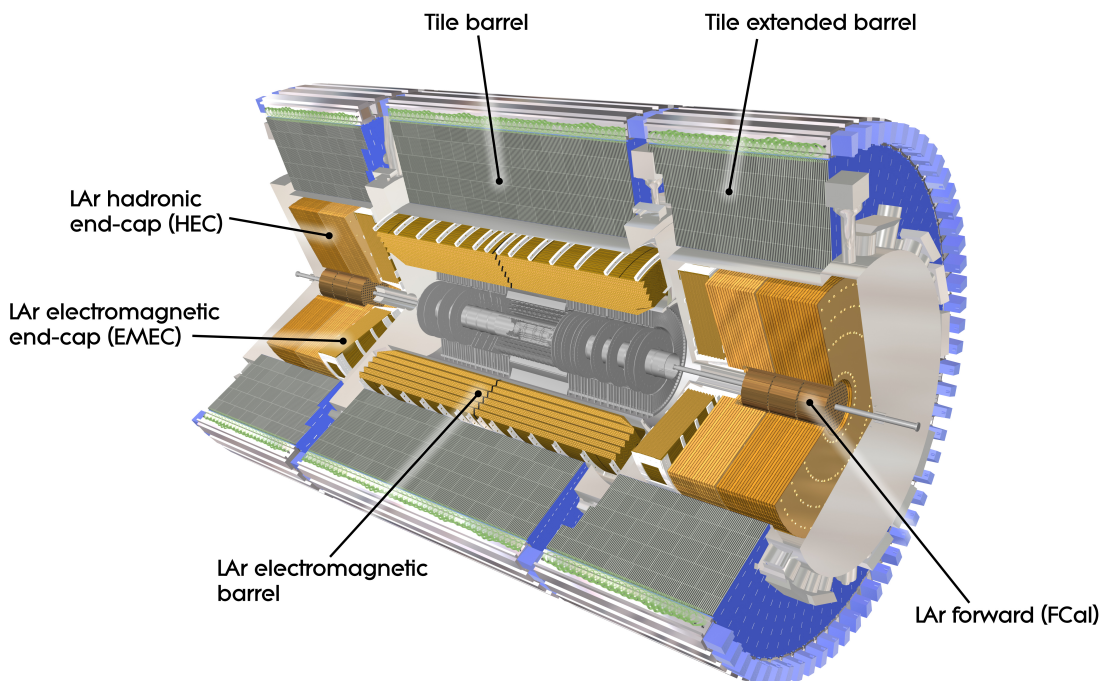


Figure 2.5: A computer generated image of the full calorimeter.

The ATLAS Calorimeter system, shown in Figure 2.5, is comprised of two main subsystems; the electromagnetic calorimeter (ECAL) and hadronic calorimeter (HCAL), which are designed to stop and measure the energy of electromagnetic-interacting and hadronic particles respectively. The combination of the two provides full coverage in ϕ and $|\eta| < 4.95$. Particles slow down and lose energy generating showers when crossing different layers. The ECAL is comprised of one barrel and two end-cap sectors employing liquid Argon (LAr). The showers hereby develop as electrons pairs which are then collected. The HCAL is also comprised of one barrel and two end-cap sectors. The sensors

in the barrel of the HCAL are tiles of scintillating plastic whereas LAr is employed for the end-cap. A forward region, the closest possible to the beam, is covered by a LAr forward calorimeter (FCal). The LAr and Tile Calorimeter will be briefly discussed in the following paragraphs.

683 The Liquid Argon Calorimeters

684 The ECAL is comprised of multiple layers of liquid Argon (LAr) sampler and lead absorber. The choice of its accordion-geometry design brought two main advantages; full ϕ coverage with no non-interactive regions (no cracks); fast extraction of signals coming from both front or rear end of the electrodes. It is made of two half-barrel wheels, both placed in the barrel cryostat, that provide a pseudorapidity coverage up to $|\eta| < 1.475$ and two end-cap detectors providing $1.375 \leq |\eta| \leq 3.20$ coverage in two end-cap cryo-stats. The junction between the barrel and end cap components defines the crack region and any signal coming from the crack region is therefore discarded.

692 In the $|\eta| < 1.8$ region there is an additional layer, placed at the front of the calorimeter, that is made of a thin (0.5 cm in the end-cap and 1.1 cm in the barrel) LAr layer with no absorber [31]. This additional layer was designed to correct for the energy lost, as particles enter the calorimeter, by taking a measurement just before the majority of the electromagnetic shower is developed.

697 The Tile calorimeter

698 The main purpose of the hadronic calorimeter is to measure the energy of hadronic showers. 699 It is built employing steel and scintillating tiles coupled to optical fibres which are read 700 out by photo-multipliers. As shown in Figure 2.5, the HCAL is made up of three cylinders; a central barrel, 5.64 m long covering a region $|\eta| < 1.0$, and two extended barrel, 702 2.91 m long covering a reigon $0.8 < |\eta| < 1.7$. Each cylinder is made up of 64 modules 703 and each module is in turn made up of three layers. Ultimately, the smallest section of the 704 calorimeter module is a cell with a $\Delta\phi \times \Delta\eta = 0.1 \times 0.1$ granularity for the two innermost 705 layers and $\Delta\phi \times \Delta\eta = 0.2 \times 0.1$ for the outermost one.

706 2.2.4 The Muon Spectrometer

707 The MS [32], shown in Figure 2.6, is the outermost sub-system of the whole ATLAS de- 708 tector. As such, it surrounds the calorimeters and its main function is to perform precision 709 measurement of muons momenta. The deflection of muon tracks employing large super-

conducting air-core toroid magnets and high-precision tracking chambers is at the heart of such high precision measurement.

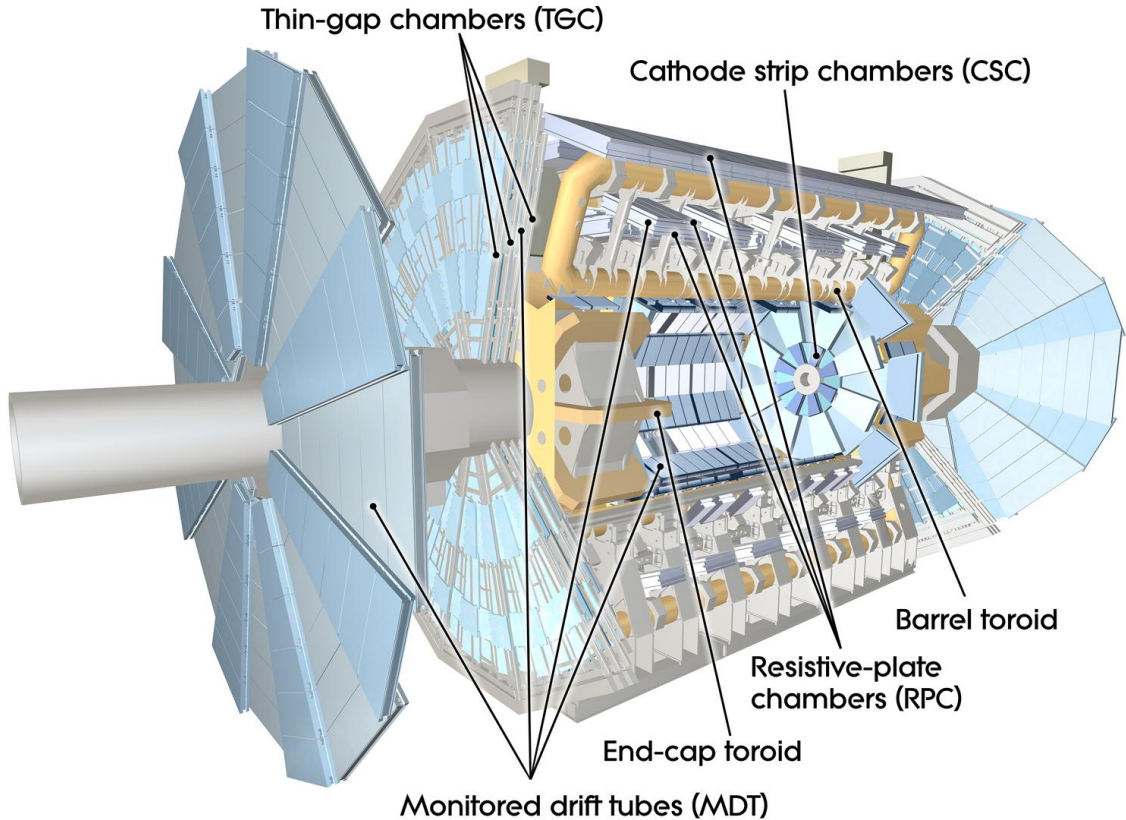


Figure 2.6: Cut-away view of the ATLAS muon system [4].

The MS is comprised of one large barrel toroid, covering the region $|\eta| \leq 1.4$, and two end-cap toroids, covering $1.6 < |\eta| \leq 2.7$ which are employed together to achieve the track-bending effect wanted. The magnitude of the magnetic field in the barrel, generated by eight large superconducting coils, ranges from 0.5 to 2 T.

Around the beam axis, three cylindrical layers make way for the chambers, placed in planes perpendicular to the beam, used to measure tracks.

Monitored Drift Chambers (MDTs) are employed over most of the pseudorapidity range to provide precision measurement of track coordinates in the bending direction. Cathode Strip Chambers (CSCs) are instead employed at large pseudorapidity ($2 < |\eta| < 2.7$). Finally, in the end-cap regions Thin-Gap Chambers (TGCs) together with Resistive-Plate Chambers (RPCs) are dedicated to the Trigger System discussed in Section 2.3.

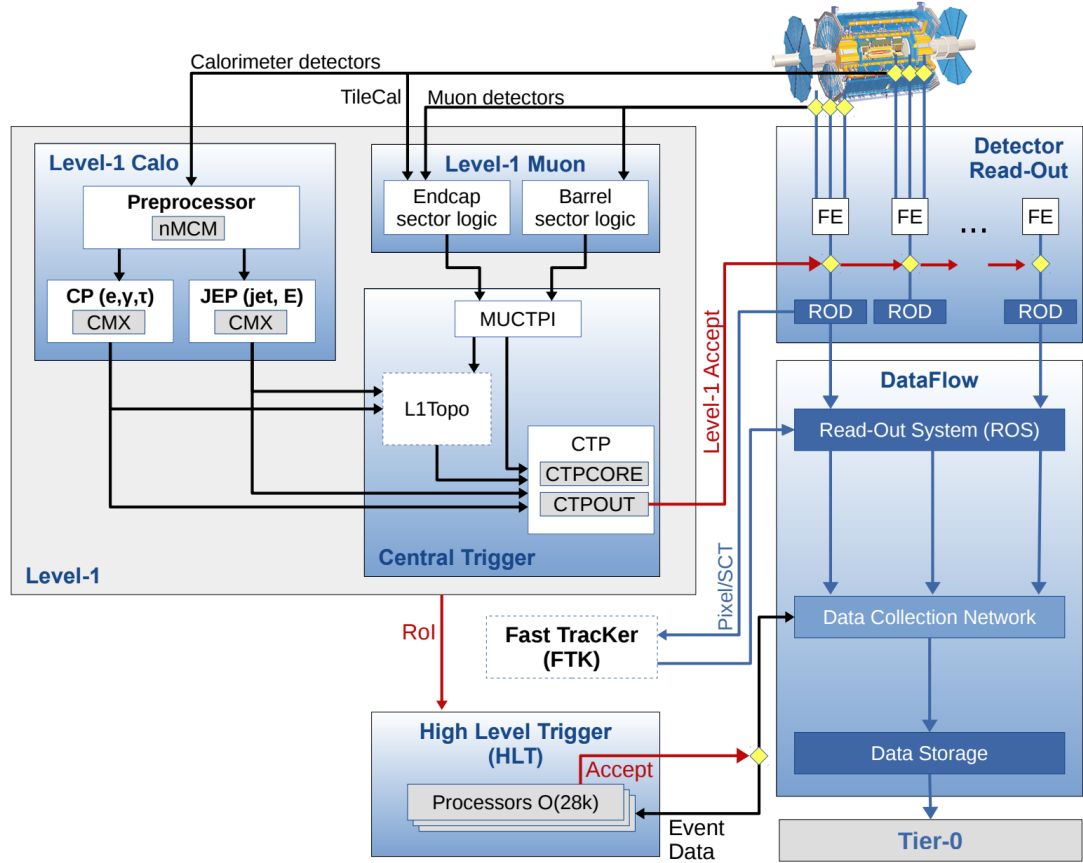


Figure 2.7: The ATLAS TDAQ system. L1Topo and FTK were being commissioned during 2015 and not used for the results shown in this thesis [5].

723 2.3 The ATLAS Trigger System

724 The ATLAS Trigger System is at the heart of data taking. It is an essential component of
725 any nuclear or particle physics experiment since it is responsible for deciding whether or
726 not to store an event for later study [5]. The ATLAS Trigger system is employed to reduce
727 the event rate from $\sim 40 \text{ MHz}$ ¹ bunch-crossing² to $\sim 200 \text{ Hz}$ which corresponds to roughly
728 300 MB/s.

729 The Trigger and Data Acquisition (TDAQ) system shown in Figure 2.7 consists of a
730 hardware-based first level trigger (L1) and a software-based high-level trigger (HLT). The
731 L1 trigger decision is formed by the Central Trigger Processor (CTP), which receives in-
732 puts from the L1 calorimeter (L1Calo) and L1 muon (L1Muon) triggers. The first level

¹ The LHC delivers beams with a bunch-spacing of 25 ns.

² The term bunch-crossing is hereby used when referring to a collision between two bunches of protons. Since only a certain fraction of the total momentum carried by each proton contributes to the collision, an average number of interactions per bunch-crossing, $\langle \mu \rangle$ is used.

733 (L1), which was designed to perform the first selection step, is a hardware-based system
 734 that uses information from the calorimeter and muon subdetectors. It also defines the
 735 so-called Regions of Interest (RoIs) within the detector to be investigated by the next level
 736 trigger, the HLT. Additionally, a Fast TracKer (FTK) system [33] (not yet installed) will
 737 provide global ID track reconstruction at the L1 trigger rate using lookup tables stored in
 738 custom associative memory chips for the pattern recognition. The FPGA-based track fitter
 739 will perform a fast linear fit and the tracks are made available to the HLT. This system will
 740 allow the use of tracks at much higher event rates in the HLT than is currently affordable
 741 using CPU systems. However, the upgrade of the ATLAS trigger will not be discussed
 742 any further.

743 In the next sections the L1 and HLT will be briefly described.

744 **2.3.1 Level 1 Trigger**

745 The Level 1 Trigger identifies Regions of Interest (RoIs)³ and passes these to HLT which
 746 will perform further investigations. Furthermore, in order to decide whether or not the
 747 event processing will continue, L1 selection uses only information coming from some
 748 parts of the detector to keep the input rate to a maximum of 100 kHz. L1 is implemented
 749 in fast custom electronics to keep the latency⁴ below $2.5 \mu\text{s}$. Event data from other sub-
 750 syststem are temporarily stored in memories whilst L1 decision is taken.

751 The L1 topological trigger (L1-Topo) [34] is feeded with energy and direction inform-
 752 ation, about the objects found by the L1 calorimeter and the muon trigger, which will be
 753 processed by dedicated algorithms implemented in its own FPGAs. However, due to the
 754 100 kHz read-out rate, not all the information collected by L1-Topo will be sent to the HLT,
 755 but only part of it. In order to properly seed the ROI-guided HLT reconstruction, specific
 756 objects in combination with the correct topological criteria must be employed.

757 **2.3.2 High-Level Trigger**

758 The HLT is used to reduce the output rate down to 1 kHz and it has a ~ 200 ms average
 759 decision time. Events that pass L1 trigger are then processed by the HLT using finer-
 760 granularity calorimeter information, precision measurements from the MS and tracking
 761 information from the ID. The HLT reconstruction can be run within RoIs identified at L1
 762 or a so-called full-scan on the full detector can be performed. The track reconstruction in

³ $\eta - \phi$ regions where event features have been found by the L1 selection process.

⁴ Time needed by an electric signal to get to the front-end electronics.

-
- ⁷⁶³ the Inner Detector is an essential component of the trigger decision in the HLT and it will
 - ⁷⁶⁴ be discussed more in detail in Chapter 3

765 **3** | The *b*-jet Trigger Signature in AT-
766 LAS

767 In this chapter the monitor and performance of the bottom-quark-initiated jet (*b*-jet) sig-
768 nature trigger, this being the author’s “technical/qualification task” to become a qualified
769 member of the experiment, will be discussed. The efficiencies of some of the Run 2 *b*-jet
770 triggers were evaluated using 3.8 fb^{-1} of pp collisions data collected in 2015 with 25 ns
771 bunch-spacing.

772 The qualification task

773 **3.1 Trigger Efficiency**

774 4 | Event Simulation and Reconstruction

775

776 bla bla bla

777 4.1 Event Generation

778 bla bla

779 4.1.1 Parton Distribution Functions (PDFs)

780 bla bla bla

781 4.1.2 Matrix Element Calculation

782 bla bla bla

783 4.1.3 Parton Showers

784 bla bla bla

785 4.1.4 Hadronisation

786 bla bla bla

787 4.2 Detector Simulation

788 bla bla bla

⁷⁸⁹ **5** | Stop searches in final states with
⁷⁹⁰ jets and missing transverse en-
⁷⁹¹ ergy

⁷⁹² 6 | Results and Statistical Interpretations

⁷⁹³

⁷⁹⁴ Trigger

⁷⁹⁵ bla vlas bla

Bibliography

- [1] ATLAS Collaboration, "Summary plots from the atlas standard model physics group." https://atlas.web.cern.ch/Atlas/GROUPS/PHYSICS/CombinedSummaryPlots/SM/ATLAS_a_SMSummary_TotalXsect/ATLAS_a_SMSummary_TotalXsect.png. viii, 9
- [2] C. Borschensky, M. Krämer, A. Kulesza, M. Mangano, S. Padhi, T. Plehn, and X. Portell, *Squark and gluino production cross sections in pp collisions at $\sqrt{s} = 13, 14, 33$ and 100 TeV*, *Eur. Phys. J.* **C74** no. 12, (2014) 3174, [arXiv:1407.5066 \[hep-ph\]](https://arxiv.org/abs/1407.5066). viii, 17
- [3] C. Lefèvre, *The CERN accelerator complex*, <http://cds.cern.ch/record/1260465>. viii, ix, 22, 23
- [4] ATLAS Collaboration, *The ATLAS experiment at the CERN Large Hadron Collider*, *Journal of Instrumentation* **3** no. 08, (2008) S08003. <http://stacks.iop.org/1748-0221/3/i=08/a=S08003>. ix, 25, 30
- [5] A. Collaboration, *Performance of the ATLAS Trigger System in 2015*, *Eur. Phys. J.* **C77** (2017), [arXiv:1611.09661 \[hep-ex\]](https://arxiv.org/abs/1611.09661). ix, 31
- [6] M. Herrero, *The Standard Model*, <https://arxiv.org/abs/hep-ph/9812242>. 2
- [7] ATLAS Collaboration, *Observation of a New Particle in the Search for the Standard Model Higgs Boson with the ATLAS Detector at the LHC*, *Phys.Lett.* **B716** (2012), [arXiv:1207.7214 \[hep-ex\]](https://arxiv.org/abs/1207.7214). 2
- [8] CMS Collaboration, *Observation of a new boson at a mass of 125 GeV with the CMS experiment at the LHC*, *Phys.Lett.* **B716** (2012), [arXiv:1207.7235 \[hep-ex\]](https://arxiv.org/abs/1207.7235). 2
- [9] A. Pich, *The Standard Model of Electroweak Interactions*, [arXiv:1201.0537 \[hep-ph\]](https://arxiv.org/abs/1201.0537). 5, 6

- 820 [10] K. A. Olive at al. (Particle Data Group), *Review of Particle Physics*, **Chin.Phys. C** **38**(9)
 821 (2014). 6
- 822 [11] J. Goldstone, A. Salam and S. Weinberg, *Broken Symmetries*, **Phys. Rev.** **127** (1962)
 823 965–970. 8
- 824 [12] S. Weinberg, *Implications of Dynamical Symmetry Breaking*, **Phys. Rev.** **D19** (1976)
 825 1277–1280. 10
- 826 [13] Super-Kamiokande Collaboration, Y. Fukuda et al., *Evidence for oscillation of
 atmospheric neutrinos*, **Phys. Rev. Lett.** **81** (1998) 1562–1567, [arXiv:hep-ex/9807003](https://arxiv.org/abs/hep-ex/9807003)
 827 [hep-ex]. 10
- 829 [14] SNO Collaboration, *Measurement of the Rate of $\nu_e + d \rightarrow p + p + e^-$ Interactions
 Produced by 8B Solar Neutrinos at the Sudbury Neutrino Observatory*, **Phys. Rev. Lett.**
 830 **87** (2001). 10
- 832 [15] T. O. W. of the Nobel Prize.
 833 https://www.nobelprize.org/nobel_prizes/physics/laureates/2015/. 10
- 834 [16] F. Jegerlehner, *The hierarchy problem of the electroweak Standard Model revisited*,
 835 [arXiv:1305.6652](https://arxiv.org/abs/1305.6652) [hep-ph]. 12
- 836 [17] A. H. Chamseddine, R. Arnowitt, and P. Nath, *Locally Supersymmetric Grand
 Unification*, **Phys. Rev. Lett.** **49** (1982) 970–974.
 837 <https://link.aps.org/doi/10.1103/PhysRevLett.49.970>. 13
- 839 [18] A. Arbey, M. Battaglia, A. Djouadi, F. Mahmoudi, and J. Quevillon, *Implications of a
 125 GeV Higgs for supersymmetric models*, **Physics Letters B** **708** no. 1, (2012) 162 – 169.
 840 <http://www.sciencedirect.com/science/article/pii/S0370269312000810>. 13
- 842 [19] L. Randall and R. Sundrum, *Out of this world supersymmetry breaking*, **Nucl. Phys.**
 843 **B557** (1999) 79–118, [arXiv:hep-th/9810155](https://arxiv.org/abs/hep-th/9810155) [hep-th]. 13
- 844 [20] G. F. Giudice, M. A. Luty, H. Murayama, and R. Rattazzi, *Gaugino mass without
 singlets*, **JHEP** **12** (1998) 027, [arXiv:hep-ph/9810442](https://arxiv.org/abs/hep-ph/9810442) [hep-ph]. 13
- 846 [21] J.M. Jowett, M. Schaumann, R. Alemany, R. Bruce, M. Giovannozzi, P. Hermes, W.
 847 Hofle, M. Lamont, T. Mertens, S. Redaelli, J. Uythoven, J. Wenninger, *The 2015
 848 Heavy-Ion Run of the LHC*,
 849 <http://accelconf.web.cern.ch/accelconf/ipac2016/papers/tupmw027.pdf>. 21

- 850 [22] O. S. Brüuning, P. Collier, P. Lebrun, S. Myers, R. Ostojic, J. Poole and P. Proudlock,
 851 *LHC Design Report*, <https://cds.cern.ch/record/782076>. 22
- 852 [23] CMS Collaboration, *The CMS experiment at the CERN LHC*, Journal of
 853 Instrumentation **3** no. 08, (2008) S08004.
 854 <http://stacks.iop.org/1748-0221/3/i=08/a=S08004>. 22
- 855 [24] LHCb Collaboration, et. al, *The LHCb Detector at the LHC*, **JINST** (2008). 22
- 856 [25] ALICE Collaboration, *The ALICE experiment at the CERN LHC*, Journal of
 857 Instrumentation **3** no. 08, (2008) S08002.
 858 <http://stacks.iop.org/1748-0221/3/i=08/a=S08002>. 22
- 859 [26] A. Yamamoto, Y. Makida, R. Ruber, Y. Doi, T. Haruyama, F. Haug, H. ten Kate,
 860 M. Kawai, T. Kondo, Y. Kondo, J. Metselaar, S. Mizumaki, G. Olesen, O. Pavlov,
 861 S. Ravat, E. Sbrissa, K. Tanaka, T. Taylor, and H. Yamaoka, *The ATLAS central*
 862 *solenoid*, Nuclear Instruments and Methods in Physics Research Section A:
 863 Accelerators, Spectrometers, Detectors and Associated Equipment **584** no. 1, (2008)
 864 53 – 74.
 865 <http://www.sciencedirect.com/science/article/pii/S0168900207020414>. 25
- 866 [27] ATLAS Collaboration, *The ATLAS Inner Detector commissioning and calibration*, **Eur.**
 867 **Phys. JC70**, [arXiv:1004.5293](https://arxiv.org/abs/1004.5293). 25
- 868 [28] ATLAS Collaboration, *ATLAS Insertable B-Layer Technical Design Report*,
 869 <https://cds.cern.ch/record/1291633>. 26
- 870 [29] G. A. et al., *ATLAS pixel detector electronics and sensors*, Journal of Instrumentation **3**
 871 no. 07, (2008) P07007. <http://stacks.iop.org/1748-0221/3/i=07/a=P07007>. 27
- 872 [30] A. Bingül, *The ATLAS TRT and its Performance at LHC*, Journal of Physics:
 873 Conference Series **347** no. 1, (2012) 012025.
 874 <http://iopscience.iop.org/article/10.1088/1742-6596/347/1/012025/meta>.
 875 28
- 876 [31] ATLAS Collaboration, *ATLAS liquid-argon calorimeter: Technical Design Report*,
 877 <https://cds.cern.ch/record/331061>. 29
- 878 [32] ATLAS Collaboration, *ATLAS muon spectrometer: Technical design report*,
 879 <https://cds.cern.ch/record/331068>. 29

880 [33] ATLAS Collaboration, *Fast TracKer (FTK) Technical Design Report*,.

881 <https://cds.cern.ch/record/1552953>. 32

882 [34] E. Simoni, *The Topological Processor for the future ATLAS Level-1 Trigger: from design to*

883 *commissioning*, [arXiv:1406.4316](https://arxiv.org/abs/1406.4316). 32